Whistler waves associated with electron beams in magnetopause reconnection diffusion regions

Shan Wang[1,2*], Naoki Bessho[1,2], Daniel B. Graham[3], Olivier Le Contel[4], Frederick D. Wilder[5], Yuri V. Khotyaintsev[3], Kevin J. Genestreti[6], Benoit Lavraud[7,8], Seung Choi[1,2], and James L. Burch[9]

[1]Astronomy Department, University of Maryland, College Park, MD, USA 20742

[2]NASA Goddard Space Flight Center, Greenbelt, MD, USA 20771

[3]Swedish Institute of Space Physics, Uppsala SE-75121, Sweden

[4]Laboratoire de Physique des Plasmas, CNRS/Sorbonne Université/Université Paris-Saclay/Observatoire de Paris/ Ecole Polytechnique Institut Polytechnique de Paris, Paris, France

[5]Department of Physics, University of Texas at Arlington, Arlington, TX, USA 76019

[6]Earth, Oceans, and Space Science, Southwest Research Institute, Durham, NH, USA 03824

[7]Institut de Recherche en Astrophysique et Planétologie, Université de Toulouse, France

[8]Centre National de la Recherche Scientifique, UMR 5277, Toulouse, France

[9]Southwest Research Institute San Antonio, San Antonio, TX 78238

*swang90@umd.edu

Key points

- In EDRs observed by MMS, electron distributions of background plus beams excite whistler by beam drift and anisotropy of both populations
- Different types of distributions and waves are inferred to depend on the distance from the X-line

- A parametric study with the linear instability analysis is used to discuss the competition between different whistler modes

Abstract

Whistler waves are often observed in magnetopause reconnection associated with electron beams. We analyze seven MMS crossings surrounding the electron diffusion region (EDR) to study the role of electron beams in whistler excitation. Waves have two major types: (1) Narrow-band waves with high ellipticities and (2) broad-band waves that are more electrostatic with significant variations in ellipticities and wave normal angles. While both types of waves are associated with electron beams, the key difference is the anisotropy of the background population, with perpendicular and parallel anisotropies, respectively. The linear instability analysis suggests that the first type of wave is mainly due to the background anisotropy, with the beam contributing additional cyclotron resonance to enhance the wave growth. The second type of distribution excites broadband waves via Landau resonance, and as seen in one event, the beam anisotropy induces an additional cyclotron mode. The results are supported by particle-in-cell simulations. We infer that the first type occurs downstream of the central EDR, where background electrons experience Betatron acceleration to form the perpendicular anisotropy; the second type occurs in the central EDR of guide field reconnection. A parametric study is conducted with linear instability analysis. A beam anisotropy alone of above ~3 likely excites the cyclotron mode waves. Large beam drifts cause Doppler shifts and may lead to left-hand polarizations in the ion frame. Future studies are needed to determine whether the observation covers a broader parameter regime and to understand the competition between whistler and other instabilities.

1. Introduction

Magnetic reconnection involves explosive energy conversion from electromagnetic fields to plasmas. In this process, highly structured particle distribution functions are formed that are unstable to various instabilities and waves to help dissipate energies and accelerate particles. The whistler wave is one example. It has $\omega_r < \omega_{ce}$ with right-hand polarization, since it is coupled to the electron gyro-motion, where the wave frequency is expressed as $\omega = \omega_r + i\gamma$. Whistlers can be excited through two modes. (1) The cyclotron mode is excited when the electron distribution has a perpendicular anisotropy that overcomes cyclotron damping (e.g., Kennel, 1966; Gurnett and Bhattacharjee, 2005), and the cyclotron resonant velocity is $v_{\parallel,res} \equiv V_{gyro} = (\omega_r \pm \omega_{ce})/k_{\parallel}$. (2) The Landau mode requires a positive slope in the distribution along $v_{||}$ ($df/dv_{||} > 0$), and the resonant velocity is $v_{\parallel,res} \equiv V_{ph,||} = \omega_r/k_{\parallel}$.

The whistler wave is commonly observed in magnetopause reconnection, and a few wave excitation mechanisms have been analyzed (e.g., review in Khotyaintsev et al., 2019). The first instability source is the anisotropy of hot magnetospheric electrons (Graham et al., 2016; Wilder et al., 2016, 2017; Le Contel, Retino, Breuillard et al., 2016; Yoo et al., 2018, Li et al., 2018, Ren et al., 2020). The corresponding waves often exhibit narrow-band power enhancements close to 0.5 f_{ce}, and statistically the waves propagate at θ_{Bn} of 10°-50° (Ren et al., 2020). In the magnetospheric inflow region on closed field lines, magnetospheric electrons can already develop a perpendicular anisotropy (e.g., Le Contel, Retino, Breuillard et al., 2016; Yoo et al., 2018). Entering the open field line region near the magnetospheric separatrix, the loss of magnetospheric electrons moving away from the X-line forms loss cone distributions that excite the waves

propagating toward the X-line (Graham et al., 2016; Wilder et al., 2017; Li et al., 2018, Zhong et al., 2021).

The picture of the whistler excitation closer to the current sheet mid-plane associated with magnetosheath populations is less clear. A statistical study of the whistler wave spectrograms shows that such waves are mainly below 0.5 f_{ce} (Ren et al., 2020). The estimated cyclotron resonance energy is often a few hundred eV, corresponding to either energized magnetosheath electrons or magnetospheric electrons (Graham et al., 2016; Le Contel et al., 2016). In an electron diffusion region (EDR) of negligible guide field reconnection, Cao et al. (2017) analyzed that the whistler wave is excited due to the perpendicular anisotropy of electrons energized in the EDR. In EDRs of guide field reconnection, field-aligned beams are often observed, and they can be associated with whistler waves (Burch, Ergun, Cassak et al., 2018; Khotyaintsev et al., 2020; Zhong et al., 2021). In an EDR with a significant guide field, Khotyaintsev et al. (2020) concluded that the magnetosheath electron beam, which has a perpendicular anisotropy, excites both an electromagnetic whistler mode through cyclotron resonance and a quasi-electrostatic oblique whistler mode through Landau resonance. The distribution can be more complicated to contain a background of energized magnetosheath-like electrons and a beam, both with perpendicular anisotropies, e.g., in an event that crossed the EDR (Burch, Webster, Genestreti et al., 2018). A model of the observed distribution was found to be unstable to whistler waves associated with the anisotropy.

Electron distributions in magnetopause reconnection diffusion regions often contain a beam concurrent with whistler waves, where the beam is usually (but not always) the magnetosheath

population. There exist studies about beam-related whistler waves for radiation belt parameters, where the beam density is very low (e.g., An et al., 2016), and for shock regions where the beam is modelled to be hotter than the background population (Wong et al., 1994). These studies showed that the beam can lead to both Landau and cyclotron resonance, and when the beam density and drift are significant**,** the drift provides a significant Doppler shift for the wave frequency. In the radiation belt regime, the electron beam/plateau can also lead to damping of the cyclotron mode whistler waves close to 0.5 f_{ce} (e.g., Chen et al., 2021, 2022). What is the role of the electron beam in exciting whistler waves in the context of magnetopause reconnection? When the beam has a perpendicular anisotropy, the anisotropy and the beam drift are two possible energy sources for the whistler instability. How do the two modes compete? In the reconnection outflow region, the beam is often superimposed on a hotter background population, which has a similar intensity with magnetosheath electrons but is usually more energized than the magnetosheath proper. For such distributions**,** what are the contributions of the individual populations to excite the whistler waves? In this study, we analyze multiple magnetopause reconnection events close to the EDR to investigate whistler waves associated with electron beams. We examine the wave properties and conduct the linear instability analysis based on the observed distributions. Additional linear instability analyses with the parameter scan are also performed to help further understand how different factors affect the instability regimes.

2. Data

Data are from the Magnetospheric Multiscale (MMS) mission burst-mode measurements. The magnetic fields are from the Flux Gate Magnetometer at 128 samples/s (Russell et al., 2016) and Search Coil Magnetometer at 8,192 samples/s (Le Contel, Leroy, Roux et al., 2016). Electric fields

are from the double probes at 8,192 samples/s (Ergun et al., 2016; Lindquvist et al., 2016; Torbert et al., 2016). Plasma data are from the Fast Plasma Investigation (Pollock et al., 2016), where the ion and electron measurements have time resolutions of 0.15 s and 0.03 s, respectively. The linear instability analysis is performed using the dispersion solver 'BO'**,** which assumes the equilibrium distribution functions to be bi-Maxwellian, and solves the dispersion relation using the matrix algorithm without requiring an initial guess of the root (Xie, 2019)**.**

3. Observations

We analyze MMS magnetopause reconnection EDR crossings. To identify EDRs, we first utilize the criteria in Lenouvel et al. (2021), with adjustments, to select candidate events. (We are not using the more sophisticated Neural Network techniques as in Lenouvel et al. (2021)). We look for data points that indicate electron current layers with electron nongyrotropy. Specifically, for magnetopause crossings with burst-mode measurements, MMS 3 data are used to look for data points that have (1) Large electron flow ($|V_{e\perp}|$ >400 km/s). (2) Electron nongyrotropy ($\frac{2(f_R-f_L)}{f_R+f_L}$>0.3), where we take the sliced distribution in the $\boldsymbol{V}_{E\times B}$ frame at the bulk $\mathbf{V}_{||}$**,** and f_R (f_L) is the average in the $v_{\perp 1} > 0 (< 0)$ half plane, with $v_{\perp 1}$ along $(\boldsymbol{B} \times \boldsymbol{V}) \times \boldsymbol{B}$. That is, a significant asymmetry exists between $v_{\perp 1} > 0$ and $v_{\perp 1} < 0$ sides. (3) Significant energy conversions ($|\boldsymbol{J} \cdot \boldsymbol{E}| > 1\, nW/m^3$). (4) Averaged to the ion time cadence, the electron perpendicular flow in the spacecraft frame is much greater than the ion perpendicular flow ($|\boldsymbol{V}_{e\perp}| - |\boldsymbol{V}_{i\perp}|)/|\boldsymbol{V}_{i\perp}| > 1$). We avoid data points that are likely in the magnetospheric inflow region by requiring (5) n>5 cm^{-3} and (6) $B_{z,GSM}$<30 nT. The numerical thresholds mentioned above are empirically determined based on the test using published events. In addition to data points that simultaneously satisfy the above six conditions, those with $\kappa^2 < 25$ are also identified, where κ^2 is the ratio of the magnetic

field curvature radius to the electron thermal gyro-radius, calculated from four-spacecraft data. The small κ^2 values indicate sharp magnetic curvatures that may cause electron demagnetization and often occur in thin current layers (e.g., Lavraud et al., 2016).

The above criteria help identify events with nongyrotropic electron current layers, and we further manually select those that have signatures of the reconnection diffusion region: (1) Parallel electron heating is a typical feature in the ion diffusion region. Thus, we look for the feature that electrons have clear parallel anisotropy in the magnetospheric inflow region. (2) Reconnection changes the magnetic field topology, and the open field lines in the outflow region enable mixture of electrons of different origins. Thus, we look for electron pitch angle distributions with asymmetries between 0 and 180 degrees in the current sheet (usually clear on the magnetospheric side). (3) Close to the X-line and on the magnetospheric side, an electric field normal to the current sheet points toward the magnetosheath (E_N>0), and it penetrates to the current sheet mid-plane (B_L~0). Further downstream, such an electric field is only restricted around the magnetospheric separatrix where B_L has large positive values. Thus, with E_N~$E_{x,GSM}$, we look for the feature that the positive $E_{x,GSM}$ (enhanced compared to a background level) penetrates to the vicinity of the current sheet mid-plane ($B_{z,GSM}$~0, where z_{GSM} is a proxy for the L direction). (4) In the EDR, the ion outflow jet is not significant, e.g., smaller than ~100 km/s of the enhancement relative to the magnetosheath level. We note that such semi-automatic methods are helpful for identifying EDR candidates, but further careful examinations are still needed for individual cases. About 10% of the events selected from the first set of criteria can pass the second set of the tests, and we further determine the LMN coordinates and examine particle distributions to finalize the event selection.

Applying the above methods to MMS dayside magnetopause crossings from 2015 fall to 2021 spring, we identify 19 EDR events, where 14 are in the list of Webster et al. (2018), 1 is in Lenouvel et al. (2021), and 5 are additional events. Other events in the Webster et al. (2018) and Lenouvel et al. (2021) lists are not included, mainly because they usually do not satisfy our criteria in the manual selection, e.g., no positive E_N penetrating to the current sheet mid-plane. Thus, these excluded events may be further away from the X-line compared with those included in this study. They are also helpful for studying whistler waves in the diffusion region, but will be left for future.

We analyze the crossings about $\pm$15 s surrounding the EDR, and can always find whistler wave packets, loosely defined by the wave power enhancements between f_{lh} (lower-hybrid frequency) and f_{ce} with right-hand magnetic field polarizations. Our interest is the effect of electron beams on exciting whistler waves, and we find 7 events that have electron beams associated with the whistler waves (Table 1). A summary of the findings is as follows. The waves and the concurrent electron distributions mainly have two types: (1) the wave is narrow-band with high ellipticity and small wave normal angle (θ_{kB}), and the instability is dominated by the perpendicular anisotropy of the background population (likely to be energized magnetosheath electrons), with the beam contributing additional cyclotron resonance to enhance the wave growth rate; (2) the wave is broad-band with more electrostatic contributions, has significant variations in the ellipticity and θ_{kB}, and the instability is associated with the Landau resonance due to the beam drift. For the second situation, the beam anisotropy may excite an additional cyclotron mode.

3.1 Whistler waves associated with anisotropy of background electrons

An example of the first type of waves is shown in Figure 1, for the EDR on 2016-11-23. The EDR is characterized by the large electron flow along both L and M directions on the magnetosheath side (B_L<0) near 07:49:34 UT. B_M is small, indicating a negligible guide field. The LMN directions in GSM are L=[0.013 0.638, 0.771], M=[0.436, -0.697, 0.570], and N=[0.900, 0.328, -0.287]. A whistler wave burst exists around 07:49:35-07:49:36 UT, which was reported in Burch, Webster, Genestreti et al. (2018), manifested as a narrow-band enhancement in the magnetic (Figure 1e) and electric (Figure 1i) field spectrograms. Wave properties are obtained from the polarization analysis (Samson and Olson, 1980). Data points that represent the whistler waves are selected with (1) the magnetic field wave power greater than 10 times of the noise level, where the noise level is determined by the average wave power spectrum in a quiet interval in the magnetosphere (2015-12-08/11:21:10 to 11:21:20 UT), and it is consistent with the noise level shown in Le Contel et al. (2016, Figure 11); (2) magnetic field degree of polarization larger than 0.7; (3) magnetic field ellipticity larger than 0.2, as shown in Figures 1f-1h. The whistler waves are in the frequency range of 0.11-0.62 f_{ce}. The waves have high ellipticities close to 1 (Figure 1f), small θ_{kB} (Figure 1g) that has an average of 24° with a standard deviation of 15°, and the wave propagation with respect to the magnetic field represented by the parallel Poynting flux ($S_{||}$) is mainly positive (Figure 1h). The location of the spacecraft is on the magnetosphere (B_L>0) -L side of the X-line with negative V_{eL} jets, so the wave propagates toward the X-line in this case.

The electron distributions concurrent with the whistler waves are examined. The pitch angle distribution for 0.2-2 keV electrons (Figure 1b) changes from counter-streaming during 07:49:34-07:49:35 UT to perpendicular anisotropy with a peak at 90° at 07:49:35-07:49:36 UT. It indicates that as the spacecraft observes the whistler waves, it is leaving the central EDR, where electrons

are energized in the perpendicular direction as the magnetic field piles up. The magnetic field indeed shows an increasing amplitude of B_N (Figure 1c). An example 2D reduced distribution during the interval marked by the vertical dashed lines (Figure 1j) shows the presence of an anti-parallel beam in addition to the background population with perpendicular anisotropy. The beam is likely a magnetosheath population moving away from the X-line. It comes across the current sheet mid-plane not too close to the EDR, so that it did not experience sufficient pitch angle scattering to become isotropic.

We model the electron distribution with two drift-bi-maxwellian distributions for the background and the beam, and use such model distributions to perform the linear instability analysis. The model distribution is obtained by fitting the 2D reduced distributions in the $v_{||} - v_{\perp 1}$ plane, with 10 fitting parameters (each drift-Maxwellian distribution has 5 parameters of n, $V_{||}$, $V_\perp$, $T_{||}$, and $T_\perp$). Figure 1k shows the modeled 2D distribution, and Figure 1l shows the comparisons between the observed (solid) and modeled (dashed) distributions for 1D cuts along $v_{||}$ (cut at $v_{\perp 1} = 0$, black) and along $v_{\perp 1}$ (cut at $v_\parallel = 0$, red), respectively. The model parameters are: (1) background n_e=12.7 cm^{-3}, $V_{e||}$=226 km/s, $V_{e\perp}$=546 km/s, $T_{e||}$=55 eV, $T_{e\perp}$=86 eV; (2) beam n_b=1.3 cm^{-3}, $V_{b||}$=-3878 km/s, $V_{b\perp}$=298 km/s, $T_{b||}$=7 eV, $T_{b\perp}$=21 eV. (The bulk $V_\perp$ of both populations are neglected in all the linear instability analyses, and we have separately confirmed that including $V_\perp$ only slightly changes the dispersion curves without changing any key conclusions.) The same distribution was modeled with four populations in Burch, Webster, Genestreti et al. (2018). Our model with two populations, although with less perfect agreement with data, captures the essence of the distribution and would help understand the roles of the background and beam populations, respectively. We also note that the resulting dispersion relation for the two-population model

qualitatively agrees with that for three- or four-population models (not shown). In addition to electrons, we model the ions as a bi-maxwellian distribution at rest with $T_{i||}$=555 eV, $T_{i\perp}$=545 eV (based on measurements), and the magnetic field strength is taken as 22 nT.

The dispersion relation for the model distribution is shown in Figure 1l where the blue and red curves represent the real and imaginary parts of the frequency, respectively. The dispersion curve is along θ_{kB}=0 with the maximum growth rate of 0.021 ω_{ce}. The corresponding real frequency is ω_r=0.23ω_{ce}, and the wavenumber is kd_e=0.63. The waves have an ellipticity of 1 (not shown). The cyclotron resonant velocity $V_{gyro} = (\omega - \omega_{ce})/k$ is about -6700 km/s, and we obtain $|V_{gyro} - V_{e||}|/v_{th||,e}$ =1.53, $|V_{gyro} - V_{b||}|/v_{th||,b}$ =1.81, where $v_{th||} = \sqrt{2k_B T_{||}/m}$. Previous studies suggested that the condition of $|V_{res} - V_{||}|/v_{th||} < \sim 2.5$ can be considered as being resonant with the whistler waves, for both the Landau and cyclotron resonance (e.g., Gary and Cairns, 1999). Thus, the right-hand polarization is consistent with the whistler waves, and the small deviations between V_{gyro} and V_e, V_b indicate that both populations contribute to the cyclotron resonance for the wave excitation.

The $\omega_r - k$ dispersion relation is modified by the drift of individual populations (mainly the beam). The purple curve is the dispersion relation for the whistler waves in the cold plasma limit with one electron population:

$$\frac{k^2c^2}{\omega^2} = \frac{\omega_{pe}^2}{\omega(\omega_{ce}\cos\theta_{kB} - \omega)} \quad (1)$$

Since the distribution involves an electron beam with a significant drift, we also plot the R-mode cold plasma dispersion relation for multiple drifting populations as the yellow curve (Stix, 1992):

$$1 - \frac{c^2k^2}{\omega^2} - \sum_s \frac{\omega_{ps}^2}{\omega^2} \frac{\omega - k_\parallel V_\parallel}{\omega - k_\parallel V_\parallel - \omega_{ce}} = 0 \quad (2)$$

The dispersion curve for the model distribution (blue) agrees with the single-electron whistler dispersion relation at small k values, and bends to have negative slopes at large k, similar to the multi-electron dispersion relation. Overall we find that the multi-electron cold plasma dispersion relation is a good approximation for the model distributions in this study. The deviation from the single-electron dispersion relation due to the drift of electron populations was also recently reported when comparing with the dispersion curve deduced from MMS measurements (Zhong et al., 2022).

To further understand the roles of the background and beam populations, we compare the growth rates of a few modified model distributions. In Figure 1m, the black curve is the growth rate same with that in Figure 1l, where both populations have perpendicular anisotropy. The blue curve is for a model that keeps the anisotropy of the background population but removes the beam anisotropy by setting its $T_\perp$ equal to $T_{||}$. The maximum growth rate is slightly smaller than the original model. The green curve is for a model that keeps the beam anisotropy and removes the background anisotropy, and the instability is suppressed. We have also confirmed that removing the beam drift has little effect on the growth rate (not shown). The result indicates that the background anisotropy dominates the whistler wave excitation, while the beam contributes to increase the growth rate.

3.2 Whistler waves associated with the beam drift via Landau resonance

An example of the second type of whistler waves is shown in Figure 2, where the EDR event was first reported in Burch and Phan (2016). The LMN directions in GSM are L=[0.265, -0.010, 0.964],

M=[0.110, -0.993, -0.041], and N=[0.958, 0.117, -0.262]. A relatively steady B_M exists throughout the shown interval, indicating the presence of the guide field. The magnetic and electric field wave spectrograms are shown in Figures 2e, and 2i, respectively. Around the time marked by the vertical dashed lines, the magnetic wave power (Figure 2e) is enhanced up to about $f_{ce}/2$, and the electric field wave power (Figure 2i) enhancement extends to higher frequencies above f_{ce}. For other wave properties shown in Figures 2f-2h, and 2j, the shown data satisfy (1) the magnetic field wave power greater than 10 times of the noise level, (2) either the magnetic field or electric field degree of polarization is greater than 0.7 and (3) the magnetic field ellipticity is greater than 0.2. Criterion 2 is less strict than that for the first type of event, since the significant electric field wave power extending to higher frequencies than the magnetic field spectrum indicates more electrostatic contributions. The selected data points are mainly below $f_{ce}/2$, covering a broad frequency range, unlike the narrow-band enhancement in the first event. The magnetic field has right-hand polarization (as required by criterion 3) with an ellipticity near 0.5 (Figure 2f), while the ellipticity of the corresponding electric field is near zero and is sometimes negative (Figure 2j).

The waveforms are further examined to ensure that the wave power enhancements are mainly due to sinusoidal wave fluctuations instead of coherent structures. Figure 2k is the DC-coupled electric field, and Figure 2l is the AC-coupled magnetic field (>1 Hz), which are up to the Nyquist frequency of 4,096 Hz. The electric field waveform exhibits high-frequency fluctuations as well as some spiky features. However, the spiky fields also have fluctuations of multiple well-defined periods, indicating that the wave power at high frequencies represents nonlinear waves rather than coherent structures. The filtered fields in the whistler wave frequency range of 50-150 and 150-500 Hz (Figures 2m-2o) exhibit regular sinusoidal fluctuations. The low-frequency portion (50-

150 Hz) of the fluctuations is mostly electromagnetic with |dE|/|dB|~10,000 km/s (close to the electron beam speed). The high-frequency portion (150-500 Hz) is more electrostatic, so only the electric field waveform is shown, and the significant $E_{||}$ fluctuations may contribute to parallel electron acceleration. The complicated electric field polarization (indicated by both the ellipticity and the waveform) was already discussed in Burch, Ergun, Cassak et al. (2018), while the frequency range and the right-hand polarized magnetic field still indicate the waves to be a type of whistler, even though the wave properties are not as clean as those for the first event. $S_{||}$ has both positive and negative values, indicating that waves propagate in both directions.

The electron distribution at the marked time shows bi-directional beams, as seen in the $v_{||}$ spectrogram (Figure 2a) and the distribution at the marked time (Figure 2p). We interpret that the spacecraft location is at the -L side of the X-line, the parallel beam is the magnetosheath population, and the anti-parallel beam is the magnetospheric population. The anti-parallel beam is as intense as the magnetosheath electrons, so it is possible that such electrons originally came from the magnetosheath, got transported to the magnetospheric side through past reconnection or waves, and serves as the magnetospheric inflow population for the current reconnection (e.g., Wang et al., 2017). Since the guide field B_M is negative, and the expected reconnection electric field E_M is also negative, the anti-parallel beam from the magnetosphere moves along +M opposite to the reconnection electric field, which can be accelerated. It might be a reason why the anti-parallel beam has a larger speed than the parallel beam.

We first model the distribution as one background population plus two beams and evaluate its corresponding linear instability condition. The model parameters are: background n_e=3.4 cm^{-3},

318 $V_{e||}$=-1113 km/s, $V_{e\perp}$=457 km/s, $T_{e||}$=115 eV, $T_{e\perp}$=99 eV; anti-parallel beam: n_{b1}=1.6 cm^{-3}, $V_{b1||}$=-
319 8967 km/s, $V_{b1\perp}$=552 km/s, $T_{b1||}$=29 eV, $T_{b1\perp}$=52 eV; parallel beam: n_{b2}=1.3 cm^{-3}, $V_{b2||}$=4115
320 km/s , $V_{b2\perp}$=1598 km/s, $T_{b2||}$=25 eV, $T_{b2\perp}$=49 eV. The model 2D distribution is shown in Figure
321 2q, with comparisons of 1D cuts with the observed distributions in Figure 2r, which well resembles
322 the data. The ions have n=6.3 cm^{-3}, $T_{i||}$=499 eV, and $T_{i\perp}$=707 eV. The magnetic field strength is
323 23 nT. We perform the linear instability analysis by neglecting the perpendicular drifts. The results
324 show that the instability grows toward the $v_{||}$<0 side, but no instability develops toward the $v_{||}$>0
325 side. The maximum growth rate occurs at θ_{kB}=148°, along which the dispersion curves are shown
326 in Figure 2s. The maximum growth rate is 0.04 ω_{ce}, at ω_r=0.36ω_{ce} and kd_e=0.69. The parallel
327 phase velocity ($V_{ph||}$) is about -5200 km/s, and $(V_{ph||} - V_{b1||})/v_{th||,b1}$=1.17, smaller than the
328 empirical threshold of the resonant condition of 2.5 (Gary and Cairns, 1999). Thus, V_{ph} is away
329 from the bulk velocity of the anti-parallel beam by about its thermal speed, so that Landau
330 resonance at $df/d|v_{||}| > 0$ contributes to the instability. The ellipticity of the waves is ~0.5,
331 which suggests that the electron gyro-motion is coupled to the waves, leading to the right-handed
332 whistler.
333
334 We next examine the instability for the distribution model only with the background and the anti-
335 parallel beam, while the parallel beam is removed. It still enables the instability, with the maximum
336 growth rate at θ_{kB}=138°. The dispersion curves are shown in Figure 2t. The maximum growth rate
337 is 0.003 ω_{ce}, occurring at ω_r=0.11 ω_{ce} and kd_e=0.25, with $(V_{ph} - V_{b1||})/v_{th||,b1}$=0.93. The
338 dispersion curves are similar if the density of the original parallel beam is added to the background
339 (not shown). It indicates that the 2-population model is also unstable to the Landau-mode whistler
340 waves, but the 3rd population of the parallel beam significantly increases the growth rate, due to

its drift. The 2-population model cannot excite a cyclotron mode whistler wave, but the cyclotron mode becomes unstable if the beam perpendicular anisotropy is increased from 1.8 to 2.6.

The distribution at the marked time is selected since it has the most prominent beam. We have also examined the instability conditions for other locations, e.g., around 11:20:44 UT. These distributions are also unstable to the Landau mode (not shown), and similar to the case above, the beam anisotropy is too small to excite the cyclotron mode wave.

3.3 Whistler waves excited by both the beam drift and beam anisotropy

Next we discuss another event where the magnetosheath beam dominates the instability, observed on 2018-02-26 (Figure 3). The LMN directions in GSM are L=[0.027, -0.265, 0.964], M=[-0.128, -0.957, -0.260], and N=[0.991, -0.116, 0.060]. The EDR is manifested with large-amplitude V_{eL} and V_{eM} (Figure 3d) during the current sheet crossing. The V_{eL} reverses the sign together with B_N, indicating that the spacecraft transitions from the +L to -L side of the X-line. Meanwhile, B_M exhibits a positive peak, likely due to the Hall field. At the positive V_{eL} side, the electron distribution exhibits parallel beams (Figure 3a), which are consistent with the motion of the magnetosheath population. Meanwhile the magnetic and electric field wave power spectrograms (Figures 3e, 3i) show broadband enhancements. The data points that represent the whistler waves in other wave properties are selected with the same criteria as in the second event on 2015-12-08. Similarly, the selected data points scatter in a broad frequency range of 0.1~0.5 f_{ce}; data are selected with positive magnetic field ellipticity, where the electric field ellipticity varies between positive and negative values; θ_{kB} is large around 45 ° with significant variations; $S_{\|}$ has both positive and negative values. The electric field waveform up to the Nyquist frequency of 4,096 Hz

(Figure 3k) exhibits high-frequency fluctuations without spiky structures, indicating that the wave power at high frequencies is contributed by additional electrostatic waves. The filtered waveforms in the whistler wave frequency range of 50-400 Hz (Figures 3m-3n) exhibit regular sinusoidal fluctuations. The two perpendicular magnetic field components (blue and green) have clear near-90° phase shifts, e.g., around 09:52:08.610 and 09:52:08.645 UT, further demonstrating the right-handed circular polarization.

A distribution at the interval marked by the vertical dashed lines (Figure 3o) is modelled and analyzed. The model 2D distribution is shown in Figure 3p, and the comparisons of 1D cuts of distributions are shown in Figure 3q, with the following parameters: background n_e=7.8 cm^{-3}, $V_{e||}$=-1029 km/s, $V_{e\perp}$=293 km/s, $T_{e||}$=90 eV, $T_{e\perp}$=57 eV; beam: n_b=3.6 cm^{-3}, $V_{b||}$=5894 km/s, $V_{b\perp}$=-170 km/s, $T_{b||}$=13 eV, $T_{b\perp}$=56 eV. The ions have n=11.4 cm^{-3}, $T_{i||}$=625 eV, and $T_{i\perp}$=653 eV. The magnetic field strength is 27 nT. Adding another population with an anti-parallel drift would further improve the agreement with data, but it does not qualitatively change the instability analysis, so we present the result for the simple background plus a beam model. Performing the linear instability analysis, we find an instability propagating toward the $v_{||}$>0 side. Figure 3r shows the dispersion curves along θ_{kB}=32°, where the maximum growth rate is 0.024 ω_{ce} occurring at ω_r=0.10 ω_{ce}, kd_e=0.33. $(V_{ph||} - V_{b||})/v_{th||,b}$ is -1.51, indicating the Landau resonance due to the beam drift. The waves have an ellipticity of ~0.7. The model distribution is also unstable to another mode propagating along θ_{kB}=180° (Figure 3s). The maximum growth rate is 0.019 ω_{ce} occurring at ω_r=0.07 ω_{ce}, and kd_e=0.79, with an ellipticity of 1. $|V_{gyro} - V_{b||}|/v_{th||,b}$=1.40, indicating that the instability is associated with the cyclotron resonance of the beam, and the free energy source is its perpendicular anisotropy. The large beam drift significantly alters the dispersion curve and

shifts ω_r to a rather small value. This situation is similar to the event reported in Khotyaintsev et al. (2020).

3.4 Implications from the observations

We may obtain some implications about the electron beam-related whistler wave properties and how they are generated close to the magnetopause reconnection EDR, illustrated in Figure 4. In the 7 events we have analyzed, 3 events have narrow-band whistler waves, and the other 4 events have broadband waves with more electrostatic contributions and more significant variations in the ellipticity and wave normal angle. The 3 narrow-band wave events all have similar background electron populations with perpendicular anisotropy, which dominates the wave generation by cyclotron resonance, where the beam contributes additional cyclotron resonance to enhance the wave growth (Figure 4, right). For the 4 broadband wave events, 3 events have a background population with a slight parallel anisotropy. The linear instability analysis suggests that such whistler waves are generated via Landau resonance (Figure 4, left), and the result is not sensitive to the electron distribution model, e.g., whether to use a model with one background plus one beam or a more accurate model with more populations. The 1 event on 2018-02-26 shown in Figure 3 is unstable to both the Landau mode and the cyclotron mode due to the beam anisotropy. The cyclotron mode has narrower ranges of ω_r and k than the Landau mode. The 1 outlier event on 2015-09-22 has a background with slight perpendicular anisotropy of 1.18. The linear instability analysis result is sensitive to the electron distribution model: it suggests Landau resonance for the background plus one beam model, and suggests cyclotron resonance if using a 3-population model. Based on these multi-event analyses, the results mostly suggest two types of waves associated with two kinds of electron distributions.

Considering the reconnection context, the two types of distributions and waves seem to be a function of the distances from the X-line. In Figure 4, the distributions are put into the reconnection context, with illustrations of the trajectories of different electron populations. The magnetosheath electron beam is often observed in the EDR, especially when a guide field (e.g., 20% or more) exists, as reported in observations (e.g., Burch and Phan, 2016; Khotyaintsev et al., 2020) and analyzed in particle-in-cell simulations (Hesse et al., 2016; Chen et al., 2017; Bessho et al., 2019; Choi et al., 2022). The beam feature can extend to outside the EDR mainly on one side of the outflow where the reconnection electric field projected to the field-aligned direction is in the direction to accelerate the beam population (e.g., Choi et al., 2022). Close to the X-line, there often co-exists a background population with parallel anisotropy, where the population can be magnetospheric electrons (Hesse et al., 2016), or it can be formed due to thermalization, e.g., by Buneman-type instabilities, as discussed in Khotyaintsev et al. (2020). Away from the X-line in the outflow direction, electrons that are trapped near the current sheet mid-plane can experience Betatron acceleration as the magnetic field becomes stronger, forming a background with perpendicular anisotropy; electrons entering the current sheet not too close to the X-line may remain as a field-aligned beam without much pitch angle scattering. Such features were discussed in magnetotail simulations and observations (e.g., Huang et al., 2015; Wang et al., 2016; Khotyaintsev et al, 2019 and references therein) and in magnetopause observations (Lavraud et al., 2016). Thus, the background population with parallel anisotropy may indicate locations close to the X-line, while the background with perpendicular anisotropy indicates a farther distance.

The role of the distance from the X-line is supported by the presented events. In the event on 2016-11-23 (Figure 1), the perpendicular anisotropy (Figure 1b) occurs when the electron flow becomes smaller, indicating that the spacecraft crossed away from the X-line. In the event on 2018-02-26 (Figure 3), the V_{eL} reversal indicates crossing of the L location of the X-line. The region with large positive V_{eL} is associated with a clear beam plus a background with parallel anisotropy. After 09:52:08.8 UT, the electron flow becomes smaller, and the perpendicular anisotropy develops along with an increasing amplitude of B_N (Figure 3b). Parallel beams co-exist with the background population as seen from the phase-space density enhancement close to zero pitch angle (Figure 3b), though the beams are weak. The whistler wave features in this event also exhibit the transition between the two types. Close to the X-line, the distribution with a background of parallel anisotropy plus a beam excites broad-band, more electrostatic waves; away from the X-line after 09:52:08.8 UT, the waves become narrow-band around 0.5 f_{ce} (Figure 3f), with higher magnetic ellipticities (Figure 3j).

4. Particle-in-cell simulations of the whistler waves based on observed parameters

In order to test whether the interpretation of the wave excitation mechanisms based on the linear instability analysis is valid, we perform 1D particle-in-cell simulations using the VPIC code (Bowers et al., 2008). The simulations have spatial variations (i.e., the wave propagation direction) along x, and start from a homogeneous magnetic field in the x-y plane. Electrons have a background population at rest (their small drift speeds in observations are neglected), and a beam population with a parallel drift. An isotropic ion population is set to have a drift such that the net current is zero. We have confirmed with the linear instability analysis that the modifications of the distributions compared to those used in the linear instability analysis in section 3 have a negligible

effect on the dispersion curves. The system size is 120 d_e with 16,128 grid cells, and the grid size of dx is in the range of 0.67~0.69 D_e and 2.7~5.9 D_b, where D_e (D_b) is the Debye length of the background (beam) electrons. A mass ratio of m_i/m_e=1836 is used. The time step is $\Delta t\omega_{pe} = 0.0074$. The number of particles per cell for each of the three populations is 10^4, with different numerical weights applied according to the density ratios.

The first case we examine is the event in Figure 1, where the background electrons have a perpendicular anisotropy of 1.6. The ratio between the electron plasma and cyclotron frequencies is $\omega_{pe}/\omega_{ce} = 50$, same as in the observation event. Since we expect the most unstable mode to be the cyclotron mode with field-aligned propagation, the magnetic field is set to be along +x, i.e., $\theta_{kB} = 0°$. The Fast Fourier Transform (FFT) spectrum as a function of k at a selected time $t\omega_{ce} = 200$ during the wave growth is shown in Figure 5a. The sign of k represents the helicity. The spectrum for k>0 is the wave power for B_y^*-iB_z^*, where the asterisk represents the FFT transformation, so the field rotates in the left-hand direction toward +x (along the background magnetic field); the spectrum at k<0 is the power for B_y^*+iB_z^*, so the field rotates in the right-hand direction toward +x. Two peaks with comparable amplitudes show up. The peak around kd_e=0.68 has a slightly higher wave power, and the value is close to the linear instability result of kd_e=0.63 for the maximum growth rate (Figure 1m). Figure 5b shows the evolution of B_z filtered in a range of kd_e=0.3 ~ 1.0. The wave fronts propagate toward +x, which together with the positive helicity indicates the right-hand polarization over time if observed at a fixed position. By tracing a wavefront as marked by the black curve, with a linear fit of the positions and time, the wave phase speed is estimated as V_{ph}=0.37 V_{Ae}. The corresponding real frequency is $\omega_r = 0.25\omega_{ce}$, close to the linear instability analysis result of $\omega_r = 0.23\omega_{ce}$, and the corresponding $V_{gyro} = (\omega -$

$\omega_{ce})/k_{||}$ is -1.10 V_{Ae}. With V_b=-0.71 V_{Ae}, $v_{th||,b}$=0.28 V_{Ae}, and $v_{th||,e}$=0.82 V_{Ae}, we estimate the gyro-resonant conditions as $(V_{gyro} - V_{b||})/v_{th||,b} = 1.4$, and $(V_{gyro} - V_{e||})/v_{th||,e} = 1.3$, so both populations satisfy the cyclotron resonant conditions. We also estimated the wave growth rate by fitting the slope between $\ln|dB|$and time during $t\omega_{ce} = 100{\sim}200$, and the results close to the power peak at positive k are shown with red dots in Figure 5a, where the correlation coefficients are required to be greater than 0.9 for the shown data points. The maximum growth rate is estimated to be $\gamma = 0.020\ \omega_{ce}$, in a good agreement with the linear instability result (Figure 1m). We note that the wave power peaks at the positive and negative k have comparable amplitudes, corresponding to waves propagating toward +x and -x respectively. It indicates that the anisotropy of the background electrons dominates the instability, and the asymmetry caused by the additional beam is not significant. In Figure 1h, the parallel Poynting flux is dominantly positive, likely because the observation location is not too close to the wave excitation location.

Next we perform simulations using the model distribution in Figure 3, where the background electrons have a parallel anisotropy $T_{e\perp}/T_{e||} = 0.6$ and the beam with $T_{e\perp}/T_{e||} = 4.3$ drifts with a speed $V_{b||}/v_{th||,b} = 3.2$. ω_{pe}/ω_{ce} is 40 according to the observation, and we first set $\theta_{kB} = 0$ to examine the possible field-aligned mode due to the beam cyclotron resonance. Figure 6a shows the FFT spectrum of the wave magnetic field as a function of k at $t\omega_{ce} = 200$, and a peak occurs at around kd_e=-0.89. The evolution of B_z shows that the wave propagates toward +x (toward the beam), which together with the negative helicity indicates that the wave is left-handed in the background electron frame. By tracing a wave front, we estimate V_{ph}=0.065 V_{Ae}. The corresponding ω_r is 0.057 ω_{ce}, V_{gyro}=1.19 V_{Ae}. With V_b=0.91 V_{Ae} and $v_{th||,b}$=0.28 V_{Ae}, the beam gyro-resonant condition is evaluated as $(V_{gyro} - V_{b||})/v_{th||,b} = 1.0$, and is hence satisfied.

Compared to the linear instability analysis in Figure 3s, the wave numbers are similar (simulation: $|k|d_e$=0.89, linear instability analysis: $|k|d_e$=0.79). The estimated growth rate by fitting data during $t\omega_{ce} = 100\sim150$ is $\gamma\sim0.04\omega_{ce}$, about twice of the linear instability analysis result of $\gamma = 0.02\omega_{ce}$. Both indicate a very small real frequency and the waves are right-handed in the resonant beam frame. However, the simulation shows a more significant frequency shift associated with the beam drift compared to the single-fluid whistler dispersion relation, so that the wave has a small V_{ph} toward the beam and the wave becomes left-handed in the background electron frame. In the observation, the low-frequency features (about $2f_{lh}$) are likely mixed with the lower-hybrid waves, and data bins with negative magnetic field ellipticities do not exhibit persistent high degree of polarizations (not shown). Therefore, the cyclotron mode wave that is expected to have a narrow frequency range and high ellipticity is not clearly observed, and it is not conclusive whether the wave is right-handed or left-handed in the background electron frame in this situation. Despite the slight difference in the real frequency that affects the wave propagation direction, the simulation result is overall consistent with the linear instability analysis.

Using the same particle distributions, we perform a simulation with $\theta_{kB} = 32°$, at which the linear instability analysis predicts the maximum growth rate for the Landau mode. The highest peak in the FFT spectrum of the magnetic field is around kd_e=0.47 (Figure 7a), slightly higher than the value of 0.33 predicted by the linear instability analysis. The growth rate is estimated to be $\gamma\sim0.01\omega_{ce}$, about half of the linear instability analysis result of $\gamma\sim0.02\omega_{ce}$. The filtered B_z at kd_e=0.3~0.9 shows that the wave propagates toward +x (Figure 7b), which together with the positive helicity indicates a right-hand polarization. The estimated V_{ph} by tracing the wave front

is 0.55 V_{Ae}. The corresponding $\omega_r = 0.26\omega_{ce}$, and $V_{ph||}$=0.65 V_{Ae}. The Landau resonant condition for the beam is satisfied with $(V_{ph||} - V_{b||})/v_{th||,b} = -0.91$.

We also examine the FFT spectrum peak around kd_e=-1.0 (Figure 7a). The filtered B_z fields at kd_e=-1.3 ~ -0.8 is shown in Figure 7c, where the wave slowly propagates toward +x with the estimated V_{ph} of 0.009 V_{Ae}. The corresponding beam gyro-resonant condition is evaluated as $(V_{gyro} - V_{b||})/v_{th||,b} = -0.16 \sim 0.38$, where the uncertainty corresponds to the kd_e range used for the calculation. It indicates the wave to be the beam cyclotron mode, similar to that in the $\theta_{kB} = 0$ case.

An additional run has been performed for $\theta_{kB} = 15°$. It also excites both the cyclotron and the Landau mode, while the cyclotron mode has a higher and dominant wave power (not shown). The relative strengths of the two modes are consistent with the expectation that the maximum growth rate for the cyclotron and Landau modes are at $\theta_{kB} = 0°$ and an oblique angle ~32°, respectively, so that the wave power for the cyclotron (Landau) mode is stronger at small (large) θ_{kB}. The results demonstrate that the Landau and the cyclotron modes can indeed be excited together.

5. Parameter scan with the linear instability analysis

To better understand the whistler wave excitation mechanisms in the magnetopause reconnection diffusion region and the role of electron beams, we perform a parameter scan using the linear instability analysis, since we have used the 1D particle-in-cell simulations to justify that such analysis is valid for predicting different modes of the whistler waves with a reasonable accuracy. Based on observations of 7 events listed in Table 1, we model the particle distributions as 1

isotropic ion population at rest, 1 background electron population at rest, and 1 electron beam with a parallel drift. We fix the magnetic field strength as 20 nT, plasma number density as 10 cm^{-3}, the ion temperature as 500 eV, and the electron beam $T_{b||}$ as 10 eV. We will scan the parameters according to their ranges obtained from the observations: the background electron $T_{e||}$ at 30-120 eV, the beam density ratio (n_b/n) mainly in the range of 0.1-0.4 (extending to 0.9 in some tests), background electron anisotropy $T_{e\perp}/T_{e||}$ at 0.5-2, beam $T_{b\perp}/T_{b||}$ mainly at 1-4. The ratio between the beam drift and beam thermal speed ($V_{b||}/v_{th||,b}$) at 1-4, where $v_{th||,b}/V_{Ae} = 0.32$. For $T_{e||}$ = 60 eV in most of the tests, it corresponds to $V_{b||}/v_{th||,e}$ of 0.4-1.6, so the beam is located around the thermal speed of the background population, and the electron distribution exhibits a bump-on-tail like property.

5.1 Background with a parallel anisotropy, Landau vs. cyclotron resonance of the beam

Let us first discuss the situation where the background electron population has $T_{e\perp}/T_{e||} \leq 1$, so that no whistler waves are generated due to the background perpendicular anisotropy. Figure 8a shows a model distribution with $T_{e||}$=60 eV, $T_{e\perp}/T_{e||}$=0.8, n_b/n=0.3, $V_{b||}/v_{th||,b}$=2, $T_{b\perp}/T_{b||}$=4. The linear instability shows that an unstable mode develops and propagates toward the $v_{||}$>0 half-plane. The maximum growth rate occurs at θ_{Bn}=48°, and the dispersion curves along this direction are shown in Figure 8c (black). The parallel phase velocity is $V_{ph||}$=2710 km/s (marked by the green dashed vertical line in Figure 8a), corresponding to $(V_{ph||} - V_{b||})/v_{th||,b}$=-0.72. It indicates the Landau resonance mechanism of exciting the whistler waves (marked as 'L' in the legend of Figure 8c and the following similar plots). Another unstable mode develops toward the $v_{||}$<0 half plane. The maximum growth rate occurs at θ_{Bn}=180°, and the dispersion curves are shown in Figure 8c (cyan). $V_{ph||}$ is -965 km/s (solid green vertical line in Figure 8a), and the cyclotron

resonant velocity is V_{gyro}=6247 km/s (solid black vertical line), which corresponds to $|V_{gyro} - V_{b||}|/v_{th||,b}$=1.32. Thus, the beam gyro-resonant condition is satisfied, and the wave is due to the beam anisotropy.. In Figure 8c, the label of 'C_b^-' indicates that the mode is due to the cyclotron resonance (C), V_{gyro} and the beam drift have the same sign (subscript of 'b'), and $V_{ph||}$ is opposite to the beam drift (superscript of '-'). Both 'L' and 'C_b^-' waves have right-hand polarization.

The instability dependence on the beam drift speed is examined by varying $V_{b||}/v_{th||,b}$ while fixing other parameters. For the Landau mode, no instability exists when $V_{b||}/v_{th||,b}$=1. Increasing $V_{b||}/v_{th||,b}$ from 2 to 2.5 increases the growth rate (Figure 8c, blue). Further increasing $V_{b||}/v_{th||,b}$, we no longer find the Landau mode; however, the cyclotron mode changes to propagate toward the beam due to the Doppler shift effect. Figure 8b shows the model distribution with $V_{b||}/v_{th||,b}$=4, where the maximum growth occurs at θ_{Bn}=30°, and $V_{ph||}$ (green vertical line) is positive. Since $V_{ph||}$ and V_{gyro} have the same sign, the waves become left-handed in the background electron frame. The corresponding dispersion curves are shown in Figure 8c (red, the superscript '+' of the label 'C_b^+' means $V_{ph||}$ is along the beam drift). Such a feature of the distribution and whistler waves was reported in a simulation study of guide field reconnection (Choi et al., 2022). Figure 8d shows the maximum growth rate as a function of $V_{b||}/v_{th||,b}$, which overall exhibits an increasing trend. The colors indicate different modes, and θ_{Bn} for the maximum growth rate is labelled. Below $V_{b||}/v_{th||,b}$=3, the oblique 'L' and parallel 'C_b^-' coexist. At $V_{b||}/v_{th||,b}$=3, the 'C_b^+' mode becomes the only instability, with parallel propagation. Further increasing $V_{b||}/v_{th||,b}$, the 'C_b^+' mode propagation becomes oblique. We have also confirmed with the 1D particle-in-cell simulations that the transition from C_b^- to C_b^+ indeed occurs at $V_{b||}/v_{th||,b}$ of 2.5~3.0 (not shown).

The dependence on n_b/n is examined and summarized in Figure 8e. $V_{b||}/v_{th||,b}$=2.5 is used, and n_b/n varies at 0.2-0.8. It shows that the Landau mode growth rate first increases and then decreases with increasing n_b/n, while the cyclotron mode growth rate increases with increasing n_b/n. We may understand the trend in the following way. The free energy of the Landau mode is the positive slope of the distribution along $v_{||}$, superposed on an overall negative slope of the background distribution. Increasing n_b/n enhances the positive slope and leads to an increase of the growth rate. However, when n_b/n is very high, the beam becomes the dominant population, and the distribution is more like a shifted beam instead of a bump-on-tail shape, so that the Landau mode becomes less favorable. Thus, we can expect that the cyclotron mode dominates when the beam density is high. For this specific set of parameters, the cyclotron mode transitions from right-hand C_b^- to left-hand C_b^+ at n_b/n=0.4, and the maximum growth rate remains at parallel propagation.

The dependence on the beam temperature anisotropy is examined and summarized in Figure 8f. We set n_b/n=0.3, $V_{b||}/v_{th||,b}$=2.5, and vary $T_{b\perp}/T_{b||}$ by changing $T_{b\perp}$. The Landau mode has increasing growth rates with increasing $T_{b\perp}/T_{b||}$ (green, blue and red curves). It can be understood that with larger $T_{b\perp}$, the region with $df/dv_{||}>0$ extends to a broader region in the velocity space, favorable for the instability. The cyclotron mode also has increasing growth rates with increasing $T_{b\perp}/T_{b||}$, as expected, since the anisotropy is the direct cause of the instability. In addition, it shows that the Landau mode dominates over the cyclotron mode at small $T_{b\perp}/T_{b||}$, e.g., 3.3, and the cyclotron mode dominates at large $T_{b\perp}/T_{b||}$, e.g., 4.

5.2 Background with perpendicular anisotropy, cyclotron modes

When the background population has perpendicular anisotropy, it further favors the anisotropy-induced whistler waves through cyclotron resonance. An example model distribution is shown in Figure 9a, where n_b/n=0.3, $V_{b||}/v_{th||,b}$=2, $T_{e\perp}/T_{e||}$=1.5, and $T_{b\perp}/T_{b||}$=2. The linear instability analysis shows that a parallel mode develops toward the beam. The dispersion curves are shown in Figure 9b (blue), with $V_{ph||}$=3399 km/s (green dashed line in Figure 9a), V_{gyro}=-8222 km/s (black dashed line), $|V_{gyro} - V_{e||}|/v_{th||,e}$=1.79. Thus, the cyclotron resonance of the background electron on the $v_{||}$ side without the beam leads to the instability (labelled as 'C_e^+' in Figure 9b). Another parallel mode develops opposite to the beam, with the dispersion curves shown in Figure 9c (blue). It has $V_{ph||}$=-1194 km/s (green solid line in Figure 9a), V_{gyro}=7624 km/s (black solid line), $|V_{gyro} - V_{e||}|/v_{th||,e}$ =1.66, and $|V_{gyro} - V_{b||}|/v_{th||,b}$ =2.06. Thus, the instability is due to the cyclotron resonance of both populations, labelled as C_b^- like before. No Landau mode with appreciable growth rates is found.

The dependence on $V_{b||}/v_{th||,b}$ is examined. Figure 9b shows that the C_e^+ mode, although the beam does not directly contribute to the cyclotron resonance, has a gradual increase of the growth rate with increasing $V_{b||}/v_{th||,b}$. Figure 9c shows that at small $V_{b||}/v_{th||,b} \leq 2$, the C_b^- mode propagates opposite to the beam (with right-hand polarization in the background frame), and the growth rate decreases as $V_{b||}/v_{th||,b}$ increases. At large $V_{b||}/v_{th||,b} \geq 3$, the Doppler shift effect makes the waves propagate toward the beam (labelled as C_b^+), represented by the negative ω_r, and the polarization becomes left-handed in the background frame. The growth rate at $V_{b||}/v_{th||,b}$=3 is smaller than those of the C_b^- modes at smaller $V_{b||}/v_{th||,b}$, while it increases as $V_{b||}/v_{th||,b}$ further increases.

Overall, the growth rate for $C_b^{-(+)}$ is larger than that of C_e^+, as the beam contributes additional cyclotron resonance to the instability. Thus, for such distributions, we may expect the waves propagating opposite to the beam are stronger than those toward the beam.

5.3 Beam-background competition

For the cyclotron mode, the anisotropy of both the background and beam populations can contribute to exciting the waves. For the observation event on 2016-11-23 (Figure 1), we showed that the instability is primarily due to the background anisotropy, since the instability still exists after removing the beam anisotropy or the beam population. For the event on 2018-02-26 (Figure 3), the beam anisotropy alone can excite a cyclotron mode. Then under what conditions can the beam anisotropy alone excite the whistler waves?

The n_b/n and $T_{b\perp}/T_{b||}$ are two important factors for beam anisotropy induced waves, and we evaluate the dependence in a quantitative way. Fixing $T_{e\perp}/T_{e||}$=1, and taking $V_{b||}/v_{th||,b}$=1, 2, 3, respectively, we vary n_b/n and $T_{b\perp}/T_{b||}$ to find critical values where the cyclotron mode starts to be unstable, defined by the growth rate threshold of 0.005 ω_{ce}. The result (Figure 10a) shows that the critical $T_{b\perp}/T_{b||}$ decreases as n_b/n increases. Increasing $V_{b||}/v_{th||,b}$ also leads to decrease of the critical $T_{b\perp}/T_{b||}$. For large n_b/n and $V_{b||}/v_{th||,b}$, there appears the C_b^+ mode that propagates toward the beam. The observed beam density ratio is typically below 0.5, so a beam anisotropy of above ~3 is needed to excite the whistler waves through cyclotron resonance.

The background temperature also affects the wave growth, since the value of the phase-space density leads to cyclotron damping. Figure 10b shows the dispersion curves for $T_{e||}$ varying at 30,

60, 90 and 120 eV, where n_b/n=0.7, $V_{b||}/v_{th||,b}$=1, $T_{e\perp}/T_{e||}$=1, and $T_{b\perp}/T_{b||}$=3. It shows that the growth rate decreases as $T_{e||}$ increases. The corresponding $V_{b||}/v_{th||,e}$ are 0.58, 0.41, 0.33, and 0.29. It is likely that with increasing $T_{e||}$, the beam location has increasing phase-space densities of the background population, which leads to more cyclotron damping and reduces the growth rate.

6. Conclusions and discussions

In this study, we investigate the whistler wave properties and excitation mechanisms related to electron beams in magnetopause reconnection diffusion regions. By analyzing 7 EDR crossings with whistler waves and electron beams, we find that the waves have two major types: (1) Narrow-band whistler waves with high ellipticity and small θ_{Bn}. (2) Broad-band whistler waves, more electrostatic, with significant variations in the ellipticity and θ_{Bn}. While the associated electron distributions of both types of waves have beams, the key difference is the anisotropy of the background population, with perpendicular and parallel anisotropies for types (1) and (2), respectively. The linear instability analysis suggests that the first type of waves is mainly due to the background anisotropy, with the beam contributing the cyclotron resonance to enhance the growth rate. The second type of waves is due to the Landau resonance associated with the beam drift, and the observed waves are often associated with large-amplitude parallel electric fields that may contribute to electron acceleration. In one event, the beam anisotropy excites a cyclotron mode in addition to the Landau mode wave. The 1D particle-in-cell simulations justify the validity of the linear instability analysis, and demonstrate that the cyclotron and Landau modes can indeed be excited simultaneously. In the reconnection context, we infer that the first type occurs downstream of the central EDR where the background population can experience Betatron

acceleration to develop the perpendicular anisotropy, and the second type of waves and distributions occur close to the central EDR of guide field reconnection.

Based on the observations, we further perform parameter scans using the linear instability analysis of model distributions, where the electron distribution model contains a background at rest and a parallel-drifting beam population.

(1) When the background has a parallel anisotropy, at small beam drifts, it excites an oblique Landau mode toward the beam and a parallel cyclotron mode opposite to the beam (if the beam has a perpendicular anisotropy). At large drifts, it excites a cyclotron mode toward the beam with left-hand polarization in the background frame. A large beam density ratio and anisotropy are overall favorable for the cyclotron mode.

(2) When the background has a perpendicular anisotropy, the anisotropy-induced whistler waves via cyclotron resonance dominates the instability. One mode has the cyclotron resonant velocity opposite to the beam, and the waves propagate toward the beam. The second mode has the cyclotron resonant velocity on the beam side, so that both populations contribute to the resonance, leading to overall higher growth rates than the other mode. When the beam drift is not too large, the second mode propagates opposite to the beam with right-hand polarization, consistent with the observations. Since the beam is mainly of magnetosheath origin, the waves would be toward (away from) the X-line on the magnetospheric (magnetosheath) side. When the beam drift is very large, the second mode could be Doppler-shifted to propagating toward the beam with left-hand polarization.

(3) To understand under what conditions the beam anisotropy alone can excite whistler waves, we have examined the critical beam density ratio and beam anisotropy for such a mode. Since the observed beam density ratio is typically below 0.5, the result suggests that the beam anisotropy needs to be above ~3. We also show that reducing the background temperature increases the wave growth rate, since it leads to less cyclotron damping.

One limitation in the observation is that the observed distributions are not really the ones that excite the observed waves. The waves may come from a different location, and the distributions may be modified after the waves are excited. The fact that the distributions concurrent with the waves are able to excite whistler waves with similar properties to the observed ones indicates that the distributions are qualitatively similar to those that really generate the waves, and that the waves are likely generated closeby. The parameter scan based on the linear instability further helps understand how variations of the distribution parameters affect the resulting waves.

Further investigations on a few aspects would be beneficial. We utilize a simplified electron distribution model of 1 background plus 1 beam. As discussed with the observation events, the distributions can be better modelled if adding additional populations, while the corresponding instabilities are qualitatively similar. Further understanding of how additional populations affect the instability would be helpful. In addition, the instability analysis suggests that when the beam density and drift are large, the Doppler shift effect leads to the cyclotron mode waves propagating toward the beam with left-hand polarization in the background electron (or ion) frame, and the corresponding real frequency is small. Such features are different from the typically observed right-hand whistler waves near $f_{ce}/2$. We do not yet find definite observational evidence of such

left-handed whistler waves in the reconnection diffusion region, and it would be valuable to examine more events to see whether the conditions can cover such a regime. Moreover, the electron distributions with a beam can be unstable to other instabilities, such as the Langmuir wave (Li et al., 2018), Buneman instability (Khotyaintsev et al., 2020), and nonlinear $E_{\parallel}$ structures (Wilder et al., 2016, 2017). These modes contribute to thermalize the distribution and change the properties of the beam and background populations. Future work is needed to understand how these additional beam-related modes compete or work together with the whistler waves and interact with particles.

Acknowledgments

Shan Wang thanks Dr. Li-Jen Chen and Dr. Keizo Fujimoto for helpful discussions. The research was supported in part by DOE Grant No. DESC0016278, NSF Grant No. AGS-2010231, NASA 80NSSC18K1369, NASA 80NSSC21K1795 and the NASA MMS mission. The French LPP involvement for the SCM instrument is supported by CNES and CNRS. MMS data are available at https://lasp.colorado.edu/mms/sdc/public/.

References

An, X., B. Van Compernolle, J. Bortnik, R. M. Thorne, L. Chen, and W. Li (2016), Resonant excitation of whistler waves by a helical electron beam, Geophys. Res. Lett., 43, 2413–2421, doi:10.1002/2015GL067126.

Bessho, N., Chen, L.-J., Wang, S., & Hesse, M. (2019), Effects of the guide field on electron distribution functions in the diffusion region of asymmetric reconnection, Phys. Plasmas, 26, 082310, https://doi.org/10.1063/1.5092809

753 Bowers, K. J., Albright, B. J., Bergen, B., Yin, L., Barker, K. J., & Kerbyson, D. J. (2008). 0.374
754 pflop/s trillion-particle kinetic modeling of laser plasma interaction on roadrunner. In
755 Proceedings of the *2008 ACM/IEEE Conference on Supercomputing* (pp. 63:1–63:11). SC '08.
756 Piscataway, NJ, USA: IEEE Press.
757 Burch, J. L., and T. D. Phan (2016), Magnetic reconnection at the dayside magnetopause:
758 Advances with MMS, Geophys. Res. Lett., 43, doi:10.1002/2016GL069787.
759 Burch, J. L., Webster, J. M., Genestreti, K. J., Torbert, R. B., Giles, B. L., Fuselier, S. A., …
760 Goldstein, J. (2018). Wave phenomena and beam-plasma interactions at the magnetopause
761 reconnection region. Journal of Geophysical Research: Space Physics, 123.
762 https://doi.org/10.1002/2017JA024789
763 Burch, J. L., Ergun, R. E., Cassak, P. A., Webster, J. M., Torbert, R. B., Giles, B. L., et al. (2018).
764 Localized oscillatory energy conversion in magnetopause reconnection. Geophysical
765 Research Letters, 45, 1237–1245. https://doi.org/10.1002/2017GL076809
766 Cao, D., et al. (2017), MMS observations of whistler waves in electron diffusion region, Geophys.
767 Res. Lett.,44,3954–3962, doi:10.1002/2017GL072703.
768 Chen, L.-J., et al. (2017), Electron diffusion region during magnetopause reconnection with an
769 intermediate guide field: Magnetospheric multiscale observations, J. Geophys. Res. Space
770 Physics, 122, 5235–5246, doi:10.1002/2017JA024004.
771 Chen, H., Gao, X., Lu, Q., Sauer, K., Chen, R., Yao, J., & Wang, S. (2021). Gap formation around
772 $0.5\Omega_e$ of whistler-mode waves excited by electron temperature anisotropy. *Journal of*
773 *Geophysical Research: Space Physics*, 126,
774 e2020JA028631. https://doi.org/10.1029/2020JA028631

775 Chen, H., Gao, X., Lu, Q., Fan, K., Ke, Y., Wang, X., & Wang, S. (2022). Gap formation around
776 0.5Ω_e in the whistler-mode waves due to the plateau-like shape in the parallel electron
777 distribution: 2D PIC simulations. *Journal of Geophysical Research: Space Physics*, 127,
778 e2021JA030119. https://doi.org/10.1029/2021JA030119
779 Choi, S., Bessho, N., Wang, S., Chen, L.-J., & Hesse, M. (2022), Whistler waves generated by
780 nongyrotropic and gyrotropic electron beams during asymmetric guide filed reconnection,
781 Phys. Plasmas, 29, 012903, doi: 10.1063/5.0059884
782 Ergun, R. E., Tucker, S., Westfall, J., Goodrich, K. A., Malaspina, D. M., Summers, D., et al.
783 (2016). The Axial Double Probe and Fields Signal Processing for the MMS Mission. Space
784 Science Reviews, 199, 167–188. https://doi.org/10.1007/s11214-014-0115-x
785 Gary, S. P., and Cairns, I. H. (1999), Electron temperature anisotropy instabilities: Whistler,
786 electrostatic and z mode, J. Geophys. Res., 104(A9), 19835– 19842,
787 doi:10.1029/1999JA900296.
788 Graham, D. B., Vaivads, A., Khotyaintsev, Y. V., & Andre, M. (2016). Whistler emission in the
789 separatrix regions of asymmetric magnetic reconnection. Journal of Geophysical Research:
790 Space Physics, 121(3), 1934–1954. https://doi.org/10.1002/2015JA021239
791 Gurnett, D. A., & Bhattacharjee, A. (2005), Chapter 9 Waves in a hot magnetized plasma, Section
792 9.3.3 Cyclotron damping, in Introduction to plasma physics, Cambridge University Press,
793 374-377.
794 Hesse, M., Y.-H. Liu, L.-J. Chen, N. Bessho, M. Kuznetsova, J. Birn, and J. L. Burch (2016), On
795 the electron diffusion region in asymmetric reconnection with a guide magnetic field,
796 Geophys. Res. Lett., 43, 2359–2364, doi:10.1002/2016GL068373.

797 Huang, C., Wu, M., Lu, Q., Wang, R., and Wang, S. (2015), Electron acceleration in the
798 dipolarization front driven by magnetic reconnection. J. Geophys. Res. Space
799 Physics, 120, 1759– 1765. doi: 10.1002/2014JA020918.
800 Kennel, C. (1966). Low-frequency whistler mode. The Physics of Fluids, 9(11), 2190–2202. Doi:
801 10.1063/1.1761588
802 Khotyaintsev, Y. V., Graham, D. B., Norgren, C., & Vaivads, A. (2019). Collisionless magnetic
803 reconnection and waves: Progress review. Frontiers in Astronomy and Space Sciences, 6(70),
804 1–20. https://doi.org/10.3389/fspas.2019.00070
805 Khotyaintsev, Y. V., Graham, D. B., Steinvall, K., Alm, L., Vaivads, A., & Johlander, A. (2020).
806 Electron heating by debye-scale turbulence in guide-field reconnection. Physical Review
807 Letters, 124(4), 045101, doi: 10.1103/PhysRevLett.124.045101
808 Lavraud, B., et al. (2016), Currents and associated electron scattering and bouncing near the
809 diffusion region at Earth's magnetopause, Geophys. Res. Lett., 43, 3042–3050,
810 doi:10.1002/2016GL068359.
811 Le Contel, O., Leroy, P., Roux, A., Coillot, C., Alison, D., Bouabdellah, A., et al. (2016). The
812 search-coil magnetometer for MMS. Space Science Reviews, 199, 257–282.
813 https://doi.org/10.1007/s11214-014-0096-9
814 Le Contel, O., Retino, A., Breuillard, H., Mirioni, L., Robert, P., & Chasapis, A. (2016). Whistler
815 mode waves and hall fields detected by mms during a dayside magnetopause crossing.
816 Geophysical Research Letters, 43(12), 5943–5952. https://doi.org/10.1002/2016GL068968
817 Lenouvel, Q., Genot, V., Garnier, P., Toledo-Redondo, S., Lavraud, B., Aunai, N., et al. (2021).
818 Identification of electron diffusion regions with a machine learning approach on MMS data at

the Earth's magnetopause. Earth and Space Science, 8, e2020EA001530. https://doi.org/10.1029/2020EA001530

Li, J., Bortnik, J., An, X., Li, W., Russell, C. T., Zhou, M., et al. (2018). Local excitation of whistler mode waves and associated Langmuir waves at dayside reconnection regions. Geophysical Research Letters, 45, 8793–8802. https://doi.org/10.1029/2018GL078287

Lindqvist, P.-A., Olsson, G., Torbert, R. B., King, B., Granoff, M., Rau, D., et al. (2016). The spin-plane double probe electric field instrument for MMS. Space Science Reviews, 199, 137–165. https://doi.org/10.1007/s11214-014-0116-9

Pollock, C., Moore, T., Jacques, A., Burch, J., Gliese, U., Saito, Y.,…Zeuch, M. (2016). Fast plasma investigation for magnetospheric multiscale. Space Science Reviews, 199, 331–406. https://doi.org/10.1007/s11214-016-0245-4

Ren, Y., Dai, L., Wang, C., Li, W., Tao, X., Lavraud, B., & Le Contel, O. (2021). Statistical characteristics in the spectrum of whistler waves near the diffusion region of dayside magnetopause reconnection. Geophysical Research Letters, 48, e2020GL090816. https://doi.org/10.1029/2020GL090816

Russell, C. T., Anderson, B. J., Baumjohann, W., Bromund, K. R., Dearborn, D., Fischer, D., Le, G., Leinweber, H. K., Leneman, D., Magnes, E. et al., The magnetospheric multiscale magnetometers, Space Sci. Rev. 199, 189–256, https://doi.org/10.1007/s11214-014-0057-3

Samson, J. C. and Olson, J. V. (1980), Some comments on the descriptions of the polarization states of waves, Geophys. J. R. Astr. Soc., 61,115–129, doi: 10.1111/j.1365-246X.1980.tb04308.x

Stix, T. H. (1992), Chapter 11 Waves in magnetized uniform media, Section 11-2 Propagation parallel to B_0, in Waves in plasmas, Springer Science & Businiess Media, 266-270.

842 Torbert, R., et al. (2016), The fields instrument suite on MMS: Scientific objectives, measurements,
843 and data products, Space Sci. Rev., 199, 105–135, doi:10.1007/s11214-014-0109-8.
844 Wang, S., L.-J. Chen, N. Bessho, L. M. Kistler, J. R. Shuster, and R. Guo (2016), Electron heating
845 in the exhaust of magnetic reconnection with negligible guide field, J. Geophys. Res. Space
846 Physics, 121, doi:10.1002/2015JA021892.
847 Wang, S., et al. (2017), Parallel electron heating in the magnetospheric inflow region, Geophys.
848 Res. Lett., 44, 4384– 4392, doi:10.1002/2017GL073404
849 Webster, J. M., Burch, J. L., Reiff, P. H., Daou, A. G., Genestreti, K. J., Graham, D. B., et al.
850 (2018). Magnetospheric Multiscale Dayside Reconnection Electron Diffusion Region Events.
851 Journal of Geophysical Research: Space Physics, 123(6), 4858–4878.
852 https://doi.org/10.1029/2018JA025245
853 Wilder, F. D., Ergun, R. E., Goodrich, K. A., Goldman, M. V., Newman, D. L., Malaspina, D. M.,
854 & Holmes, J. C. (2016). Observations of whistler mode waves with nonlinear parallel electric
855 fields near the dayside magnetic reconnection separatrix by the magnetospheric multiscale
856 mission. Geophysical Research Letters, 43(6), 5909–5917.
857 https://doi.org/10.1002/2016GL069473
858 Wilder, F. D., Ergun, R. E., Newman, D. L., Goodrich, K. A., Trattner, K. J., Goldman, M. V., &
859 Lindqvist, P.-A. (2017). The nonlinear behavior of whistler waves at the reconnecting dayside
860 magnetopause as observed by the magnetospheric multiscale mission: A case study. Journal
861 of Geophysical Research: Space Physics, 122(5), 5487–5501.
862 https://doi.org/10.1002/2017JA024062
863 Wilder, F. D., Ergun, R. E., Hoilijoki, S., Webster, J., Argall, M. R., Ahmadi, N., & Giles, B. L.
864 (2019). A survey of plasma waves appearing near dayside magnetopause electron diffusion

region events. Journal of Geophysical Research: Space Physics, 124(10), 7837–7849. https://doi.org/10.1029/2019JA027060

Wong, H. K., and Smith, C. W. (1994), Electron beam excitation of upstream waves in the whistler mode frequency range, J. Geophys. Res., 99(A7), 13373– 13387, doi:10.1029/94JA00821.

Xie, H. (2019), BO: A unified tool for plasma waves and instabilities analysis, Comput. Phys. Commun. 244, 343–371, https://doi.org/10.1016/j.cpc.2019.06.014

Yoo, J., Jara-Almonte, J., Yerger, E., Wang, S., Qian, T., Le, A., et al. (2018). Whistler wave generation by anisotropic tail electrons during asymmetric magnetic reconnection in space and laboratory. Geophysical Research Letters, 45, 8054 – 8061. https://doi.org/10.1029/2018GL079278

Zhong, Z. H., Graham, D. B., Khotyaintsev, Y. V., Zhou, M., Le Contel, O., Tang, R. X., & Deng, X. H. (2021). Whistler and broadband electrostatic waves in the multiple X-line reconnection at the magnetopause. Geophysical Research Letters, 48, e2020GL091320. https://doi.org/10.1029/2020GL091320

Zhong, Z. H., Zhou, M., Graham, D. B., Khotyaintsev, Y. V., Wu, Y. F., Le Contel, O., et al. (2022). Evidence for whistler waves propagating into the electron diffusion region of collisionless magnetic reconnection. Geophysical Research Letters, 49, e2021GL097387. https://doi.org/10.1029/2021GL097387

Table 1 List of model distribution parameters for the whistler wave events

Time	B (nT)	n (cm^{-3})	$T_{e\parallel}$ (eV)	$T_{b\parallel}$ (eV)	$\frac{n_b}{n}$	$\frac{V_{b\parallel}}{v_{th\parallel,b}}$	$\frac{V_{b\parallel}}{V_{Ae}}$	$\frac{T_{e\perp}}{T_{e\parallel}}$	$\frac{T_{b\perp}}{T_{b\parallel}}$	mechanism
20150919/074447	29	23.1	26	5	0.13	2.23	0.52	1.85	4.00	Background anisotropy
20151022/060527	21	12.7	63	5	0.07	3.49	0.84	1.29	3.80	Background anisotropy
20161123/074935	22	14	55	7	0.09	2.47	0.71	1.56	3.00	Background anisotropy
20151208/102149	20	5.7	85	15	0.35	1.74	0.51	1.18	2.67	Anisotropy/Landau
20150922/134125	23	5.6	64	30	0.46	1.91	0.68	0.89	1.93	Landau, Msh beam
20151208/112043	23	5	115	29	0.32	2.46	0.81	0.86	1.79	Landau, Msph beam
20180226/095208	27	11.4	90	13	0.32	3.24	0.91	0.63	4.31	Landau, Msh beam; beam anisotropy

$V_{b\parallel}$ represents the relative drift between the background and the beam. It can be characterized by either $V_{b||}/v_{th||,b}$ or $V_{b||}/V_{Ae}$, and both values are provided. For these observation events, the background does not always have zero drift, and we keep their drift velocities in the model. 'Msh' represents 'Magnetosheath', 'Msph' represents 'Magnetospheric'

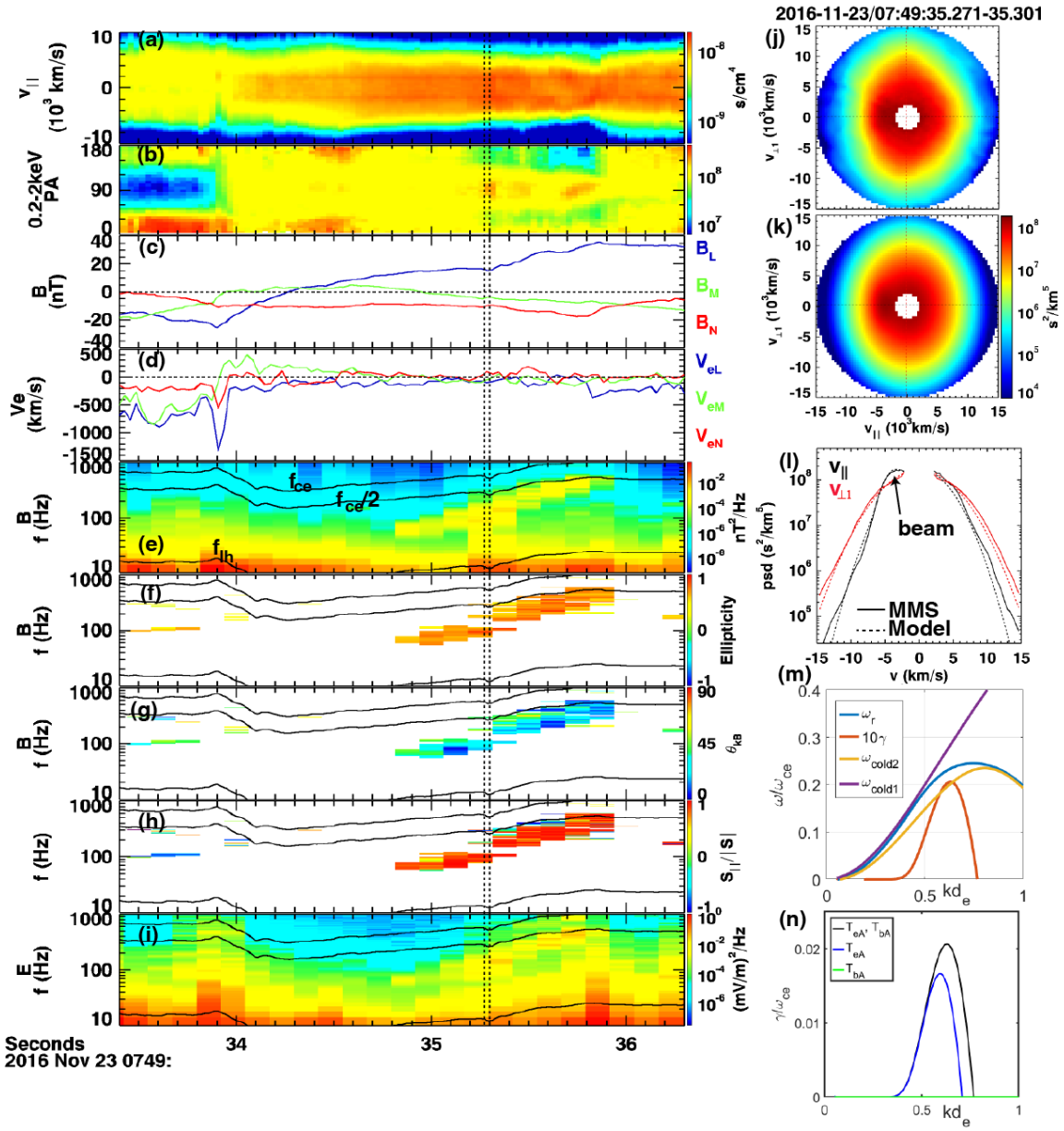

Figure 1. Narrow-band whistler wave observation in the EDR crossing on 2016-11-23 by MMS1. (a) Electron reduced 1D spectrograms along $v_{||}$. (b) Pitch angle distributions of 0.2-2 keV electrons (the energy range for energized magnetosheath populations). (c) Magnetic field. (d) Electron bulk velocity, with large values around 07:49:34 UT that indicate the EDR crossing. (e) Magnetic field FFT wave power spectrogram. The narrow-band enhancements below $f_{ce}/2$ during 07:49:35-07:49:36 UT indicate the whistler wave. (f) Magnetic field ellipticity. (g) Magnetic field wave normal angle. (h) Parallel Poynting flux normalized by the Poynting flux amplitude, indicating the propagation direction. (i) Electric field wave power spectrogram. For (f)-(h), data with the magnetic field degree of polarization greater than 0.7, magnetic field ellipticity greater than 0.2 are shown, which represent the whistler wave. (j) The observed 2D reduced electron distribution during the vertical dashed lines marked in the left panels. (k) The modeled distribution using one background population plus one electron beam. (l) Comparison of observed (solid) and modeled

(dashed) 1D cuts of the reduced distributions along $v_{||}$ (black) and $v_{\perp 1}$ (red). (m) The dispersion curves based on the model distributions, blue: real frequency; red: 10 times of the growth rate; purple: the theoretical cold plasma whistler wave dispersion relation based on the single-electron population; yellow: the R-mode cold plasma dispersion relation for two drifting electron populations, which resemble the features in the real frequency curve. (n) The growth rate for the original model in (k) where both populations have perpendicular anisotropy (black), a model that has anisotropy only for the background electrons (blue), a model that has anisotropy only for the beam (green).

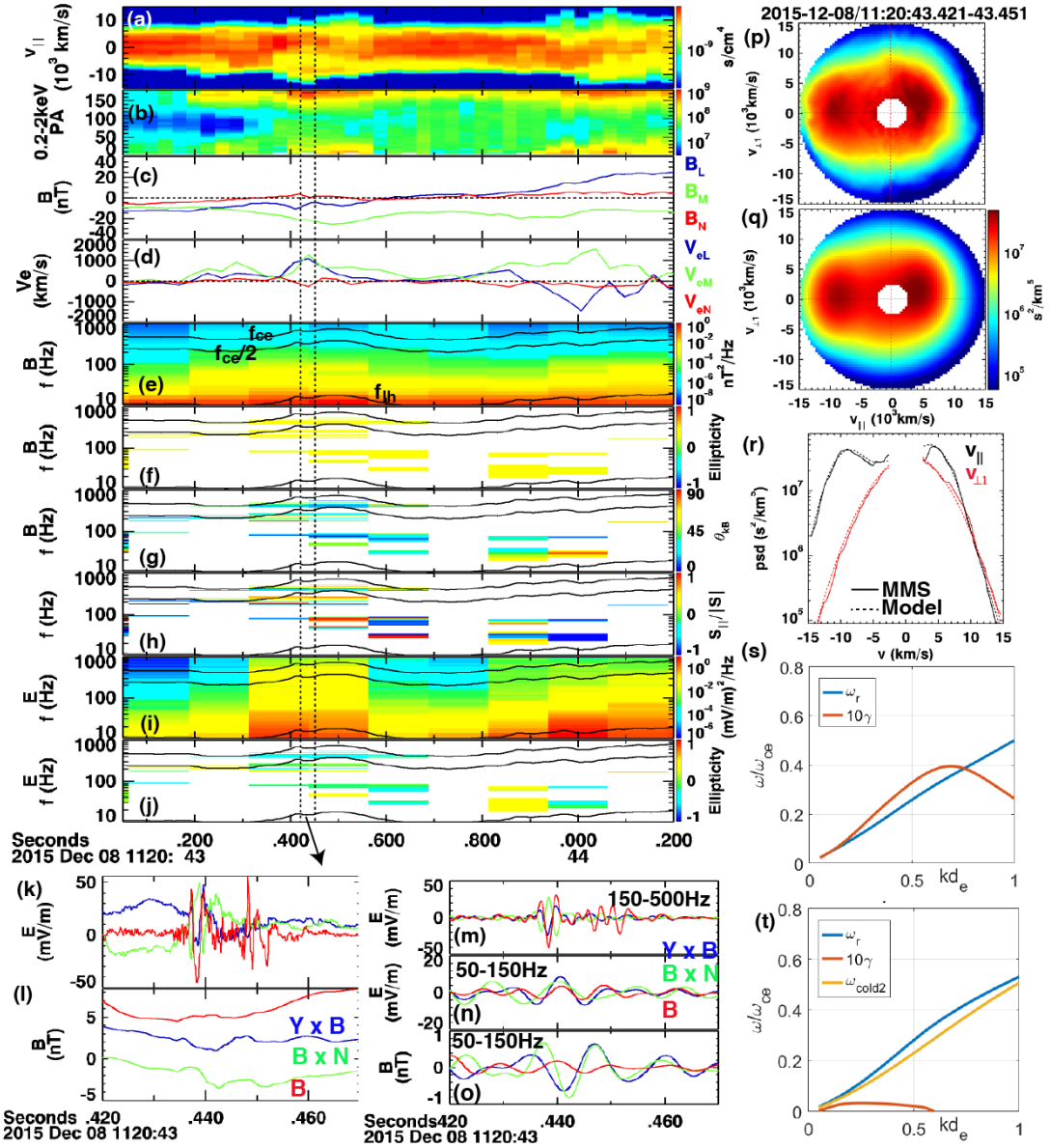

Figure 2. Broad-band more electrostatic whistler wave observation in the EDR on 2015-12-08 by MMS2. (a)-(i) The formats are the same as in Figures 1a-1i. (j) Electric field ellipticity. The criteria of the selected data points in (f)-(h), (j) are less restrict than in Figure 1, where either the magnetic or electric field degree of polarization needs to be greater than 0.7, and the magnetic field ellipticity needs to be greater than 0.2. (k) DC-coupled electric field waveforms in the field-aligned coordinate up to the Nyquist frequency of 4,096 Hz. (l) AC-coupled magnetic field (>1 Hz) waveforms up to 4,096 Hz. The waveforms at the whistler frequency range of the electric field at 150-500 Hz (m) and electric and magnetic field at 50-150 Hz (n)-(o) show that the wave power enhancements are associated with sinusoidal fluctuations instead of purely due to the coherent structures. (p) Observed distribution during the marked vertical dashed lines. (q) The model distribution with one background and two electron beams. (r) Comparisons of 1D cuts of distributions between the observation and the model. (s) The dispersion curves for the 3-population model in (q). (t) The dispersion curves for a model that only has the background and the $v_{||}<0$ beam.

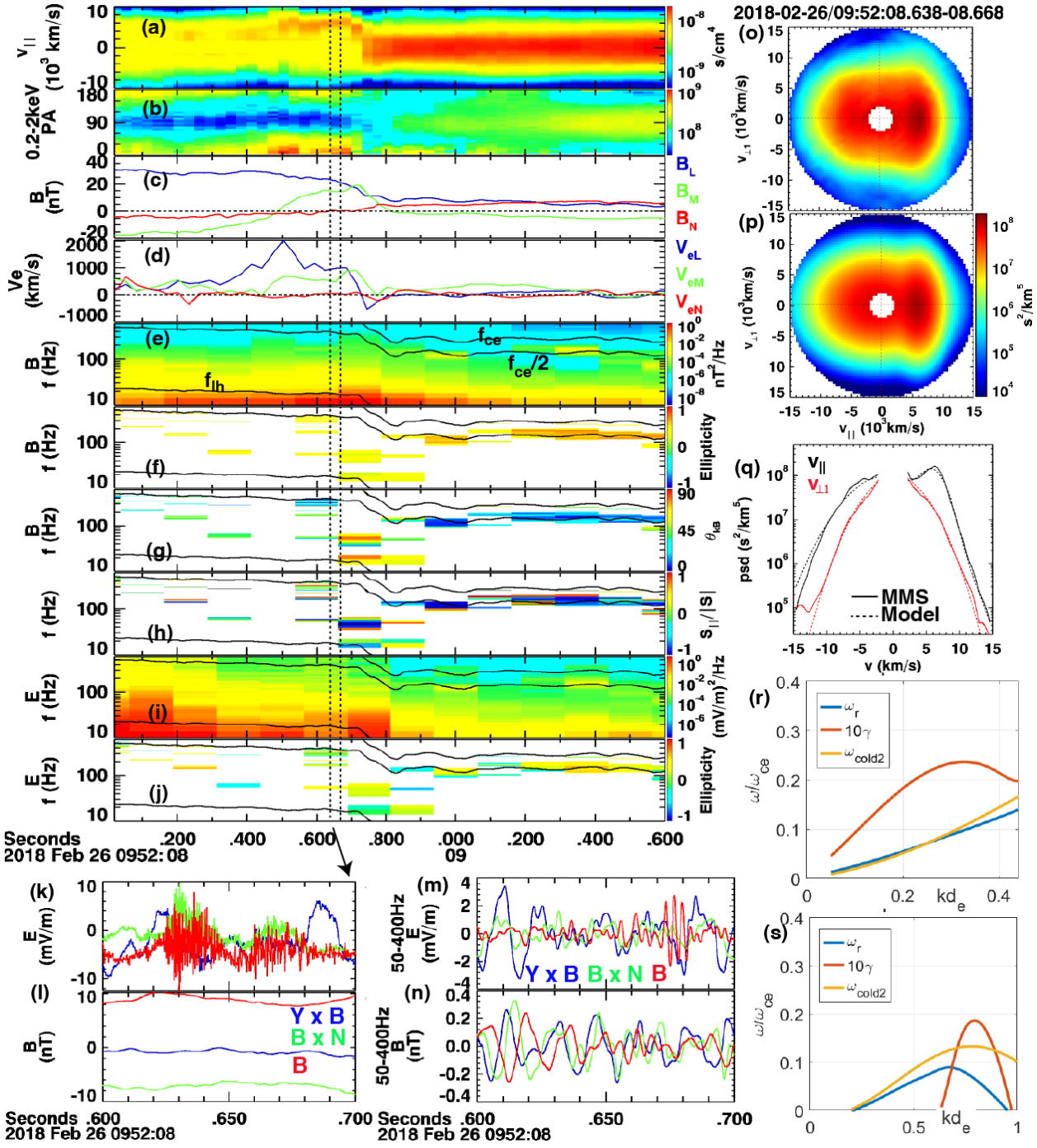

Figure 3. Broad-band whistler wave observation in the EDR on 2018-02-26 by MMS 3. (a)-(n) The formats are the same as in Figures 2a-2n. (o) Observed distribution during the marked vertical dashed lines. (p) The model distribution with one background and one beam. (q) Comparisons of 1D cuts of distributions between the observation and the model. (r) Dispersion curves for the Landau mode wave excited by the model distribution in (p), propagating at θ_{kB} =32°. (s) Dispersion curves for the cyclotron mode wave excited by the model distribution, propagating at θ_{kB}=180°. Electrons exhibit transitions from a background with parallel anisotropy plus a beam to a background with perpendicular anisotropy plus a weak beam, indicating a crossing away from the central EDR. The corresponding whistler waves transition from broad-band to narrow-band.

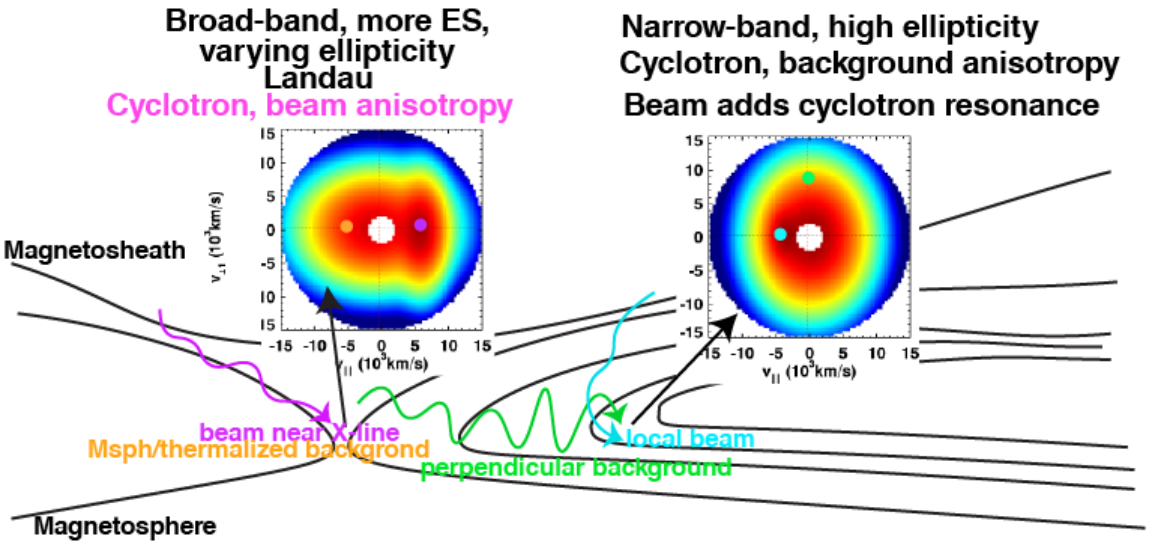

Figure 4. Illustration of the waves and electron distributions in the magnetopause reconnection context. Colored trajectories represent the behaviors of populations marked by dots of the same color in the distributions. The distribution with a background population that has slight parallel anisotropy plus a beam is likely to be close to the X-line. The corresponding waves are broad-band with a significant electrostatic component, due to Landau resonance. The beam anisotropy can also excite a (narrow-band) cyclotron mode, as demonstrated in the observation event in Figure 3. The distribution with a background that has perpendicular anisotropy plus a beam may be at further downstream locations, where the background experienced Betatron acceleration and the beam locally enters the current sheet. The corresponding wave is narrow-band with high ellipticity, due to cyclotron resonance dominant by the background anisotropy.

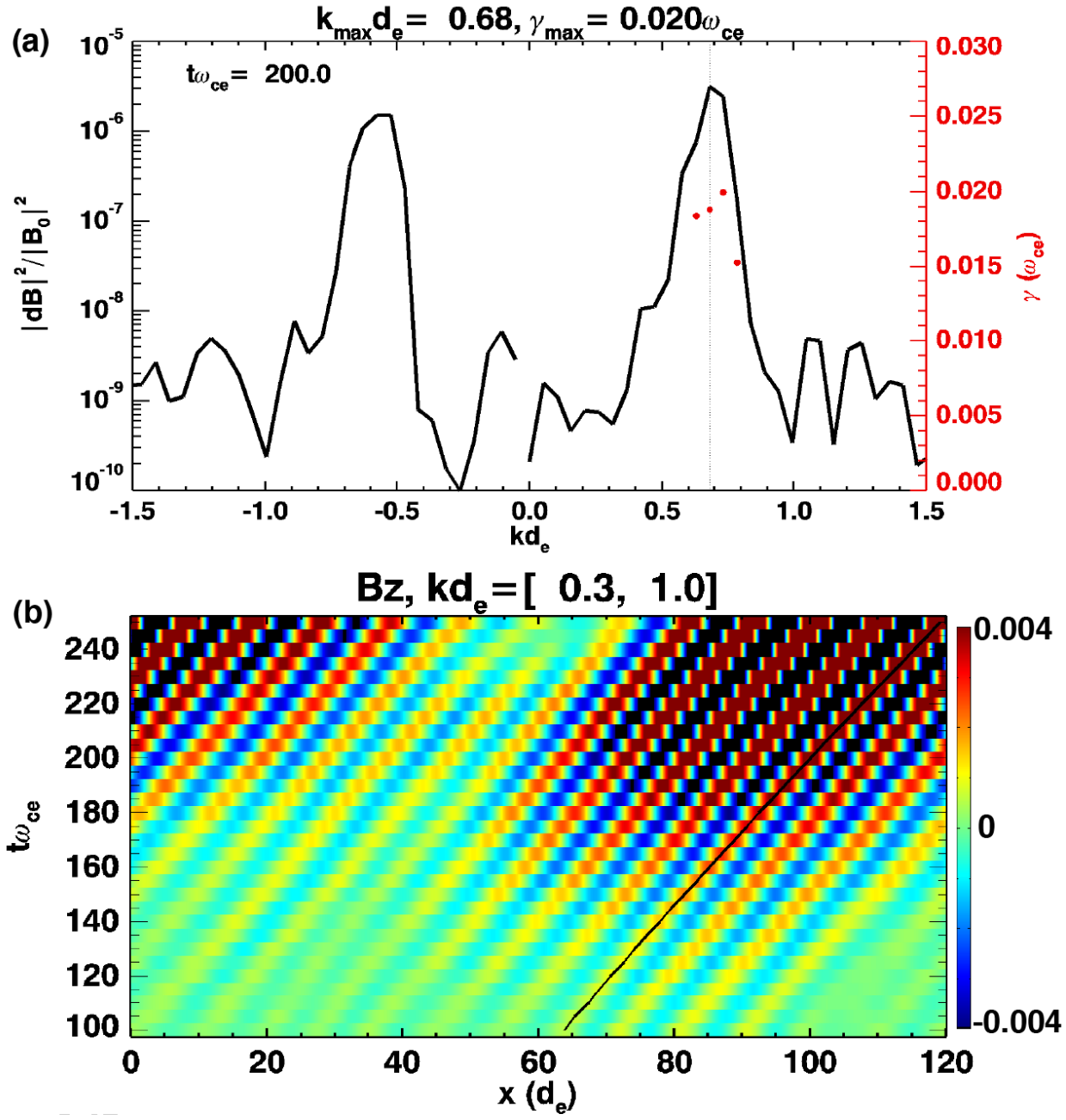

Figure 5. The 1D particle-in-cell simulation result based on the model distribution in Figure 1, where the background electrons have a perpendicular anisotropy, with $\theta_{kB} = 0$. (a) FFT spectrum (black) of the wave magnetic field as a function of k at $t\omega_{ce} = 200$, where the sign of k indicates the helicity. The red dots represent the estimated growth rates by fitting the growth rate of the magnetic field wave power at $t\omega_{ce} = 100\sim200$. (b) The time evolution of the filtered B_z in a range of kd_e=0.3~1.0. The wave propagation toward +x parallel to the background magnetic field together with the positive helicity indicates the right-hand polarization. The wave properties have a good consistency with the linear instability analysis result in Figure 1.

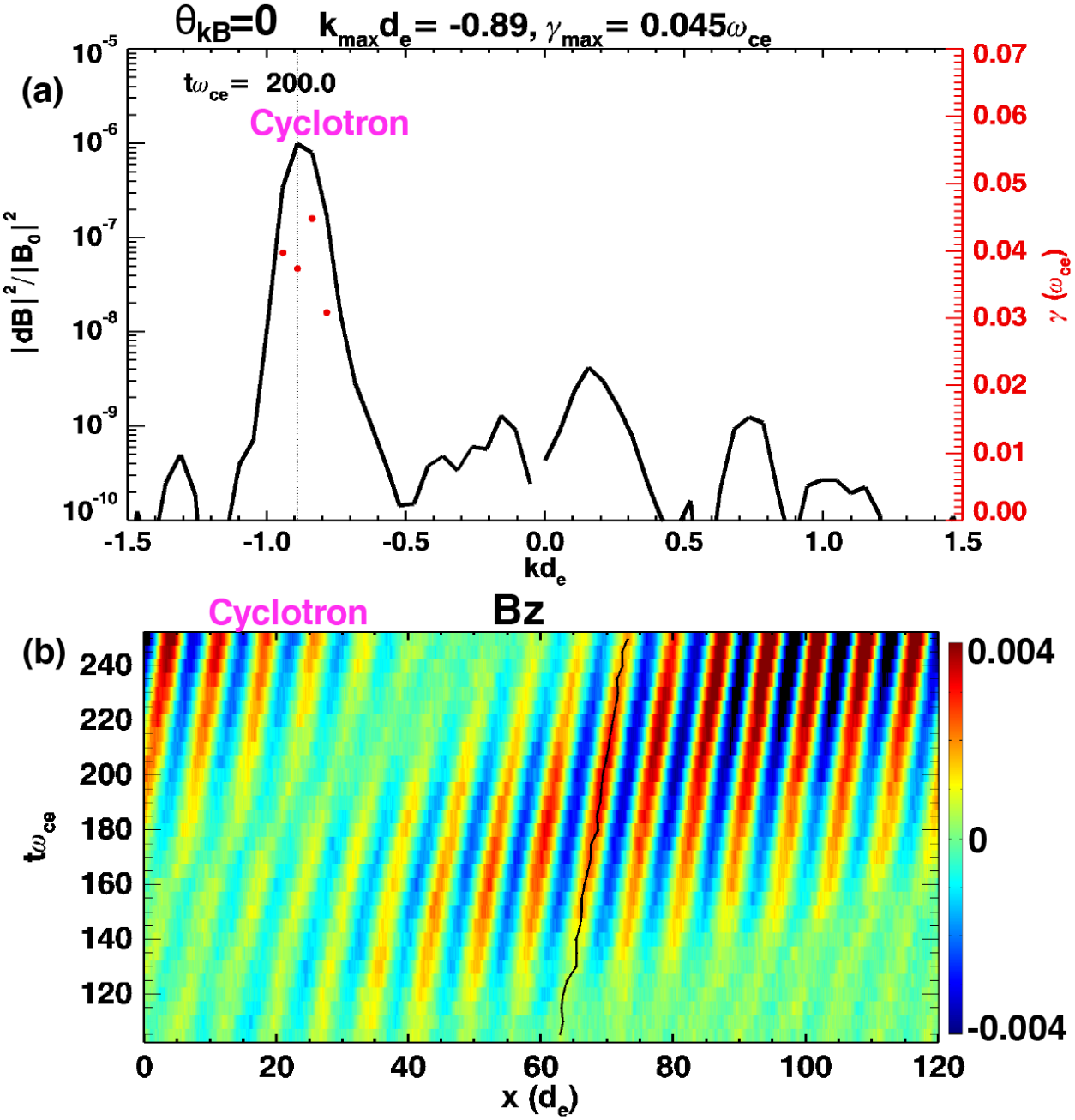

Figure 6. The 1D particle-in-cell simulation result for the model distribution in Figure 3, with $\theta_{kB} = 0$. (a) FFT spectrum (black) of the wave magnetic field as a function of k at $t\omega_{ce} = 200$. The red dots represent the estimated growth rate for $t\omega_{ce} = 100{\sim}150$. (b) The B_z evolution. The result is consistent with the beam cyclotron mode.

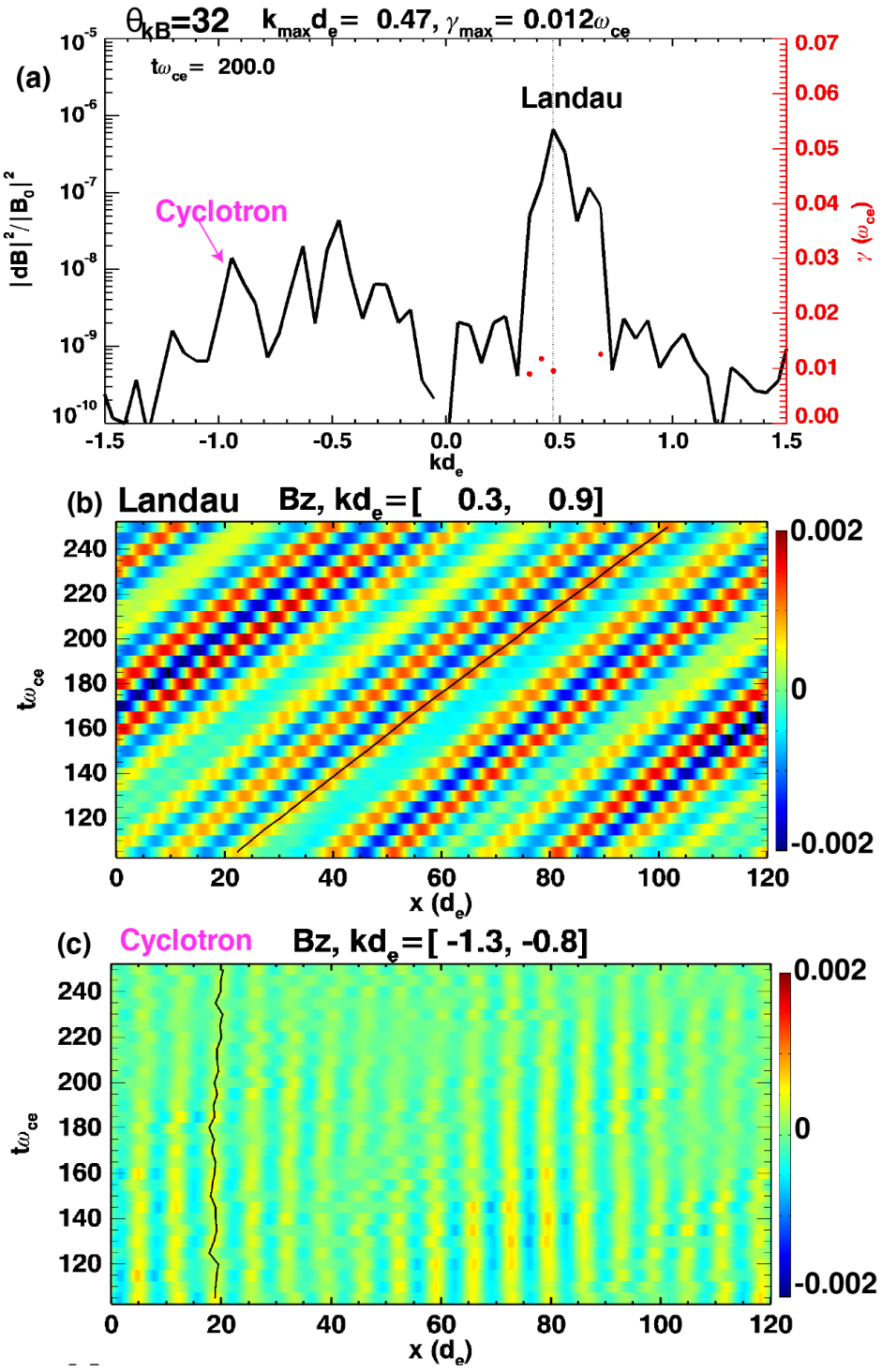

964

965 **Figure 7.** The 1D particle-in-cell simulation result for the model distribution in Figure 3, with
966 $\theta_{kB} = 32°$. The dominant wave power peak in the FFT spectrum (a, black) is consistent with the
967 Landau mode, with the filtered B_z evolution shown in (b). The red dots represent the estimated
968 growth rate for $t\omega_{ce} = 90{\sim}140$. A secondary wave power peak around kd_e=-1.0 has the
969 corresponding B_z evolution shown in (c), which is consistent with the beam cyclotron mode that
970 co-exists with the Landau mode.

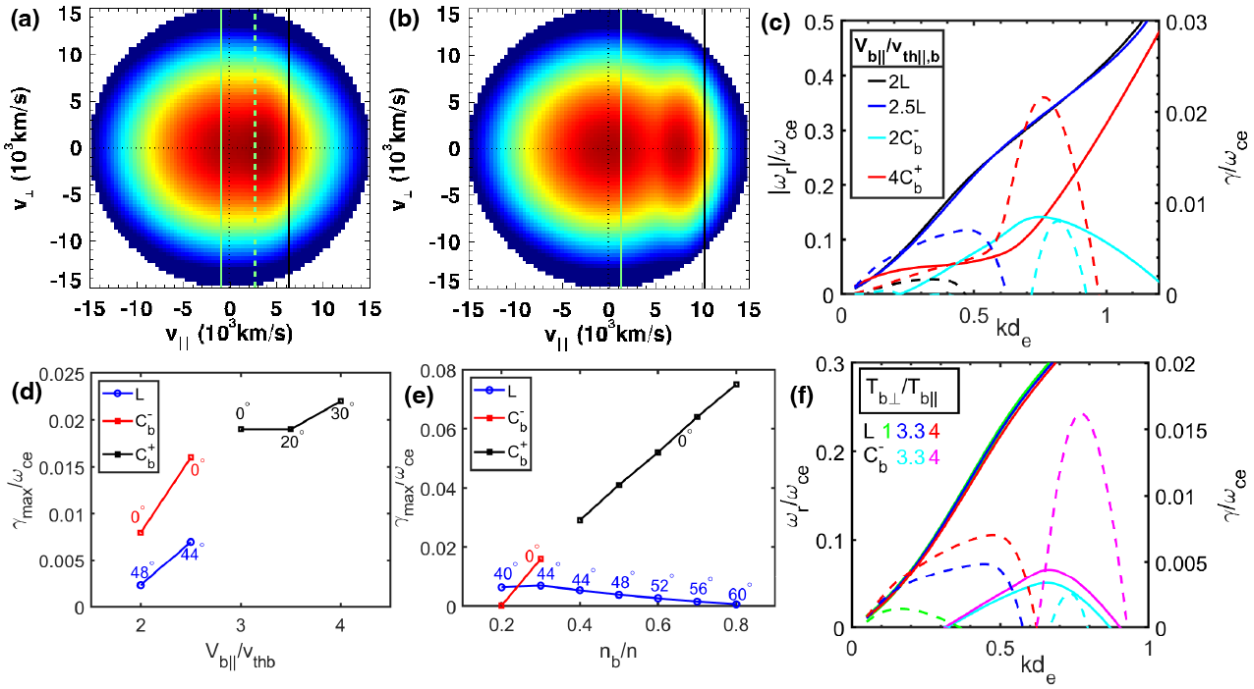

Figure 8. The linear instability analysis for model distributions of a background electron population with parallel anisotropy plus a beam. (a) An example 2D reduced distribution with n_b/n=0.3, $V_{b||}/v_{th||,b}$=2, $T_{e\perp}/T_{e||}$=0.8, and $T_{b\perp}/T_{b||}$=4. The green dashed vertical line marks $V_{ph,||}$ of the Landau mode toward the beam. The solid green line marks $V_{ph,||}$ of the cyclotron mode propagating opposite to the beam, and the solid black line marks the cyclotron resonance velocity V_{gyro}. (b) An example distribution with same parameters as in (a) except for $V_{b||}/v_{th||,b}$=4. The solid green line marks $V_{ph,||}$ of the cyclotron mode propagating toward the beam, and the solid vertical line marks V_{gyro}. (c) Dispersion curves for four cases. For all the similar figures that follow, the solid curves are for the real frequency with the values shown on the left axis, and dashed curves are for the growth rate with the values shown in the right axis. In the labels, the numbers represent the values of $V_{b||}/v_{th||,b}$; 'L' represents the Landau mode; 'C' represents the cyclotron mode; the subscript 'b' indicates that V_{gyro} has the same sign with the beam drift; the superscript '+' or '-' represents whether the wave propagates toward or opposite to the beam. (d) The maximum growth rate as a function of $V_{b||}/v_{th||,b}$, with n_b/n=0.3. Colors represent different modes, and marked numbers represent θ_{Bn} for the maximum growth rate of each mode. (e) The maximum growth rate as a function of n_b/n, with $V_{b||}/v_{th||,b}$=2.5. (f) Dispersion curves for different $T_{b\perp}/T_{b||}$, with n_b/n=0.3, and $V_{b||}/v_{th||,b}$=2.5.

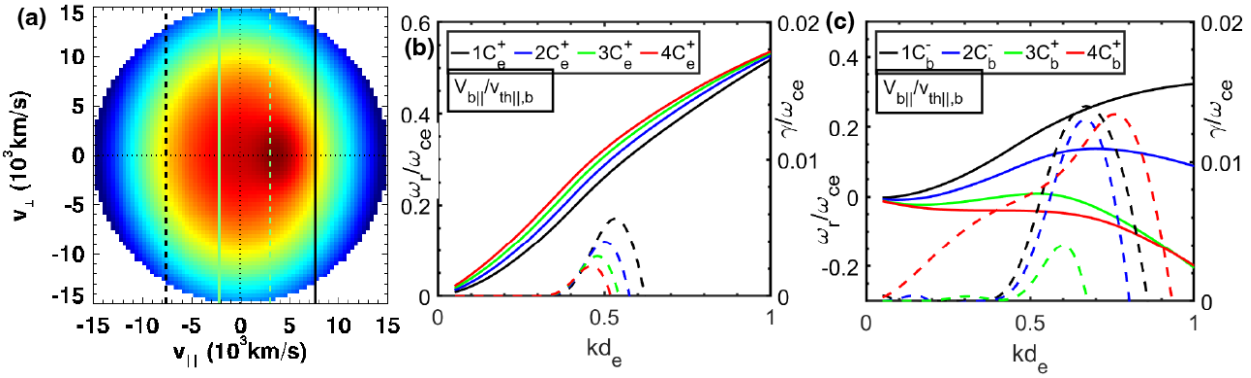

989

990 **Figure 9.** The linear instability analysis for model distributions of a background electron
991 population with perpendicular anisotropy plus a beam. (a) A model distribution with n_b/n=0.3,
992 $V_{b||}/v_{th||,b}$=2, $T_{e\perp}/T_{e||}$=1.5, and $T_{b\perp}/T_{b||}$=2. (b) Dispersion curves for modes with V_{gyro} on the
993 side with only the background electrons without a beam (indicated by the subscript of 'e' in the
994 labels). The $V_{ph,||}$ (green) and V_{gyro} (black) of the example distribution (a) are marked with dashed
995 lines. (c) Dispersion curves for modes with V_{gyro} on the side with the beam (indicated by the
996 subscript of 'b' in the labels). $V_{ph,||}$ and V_{gyro} of the example distribution (a) are marked with solid
997 lines.
998

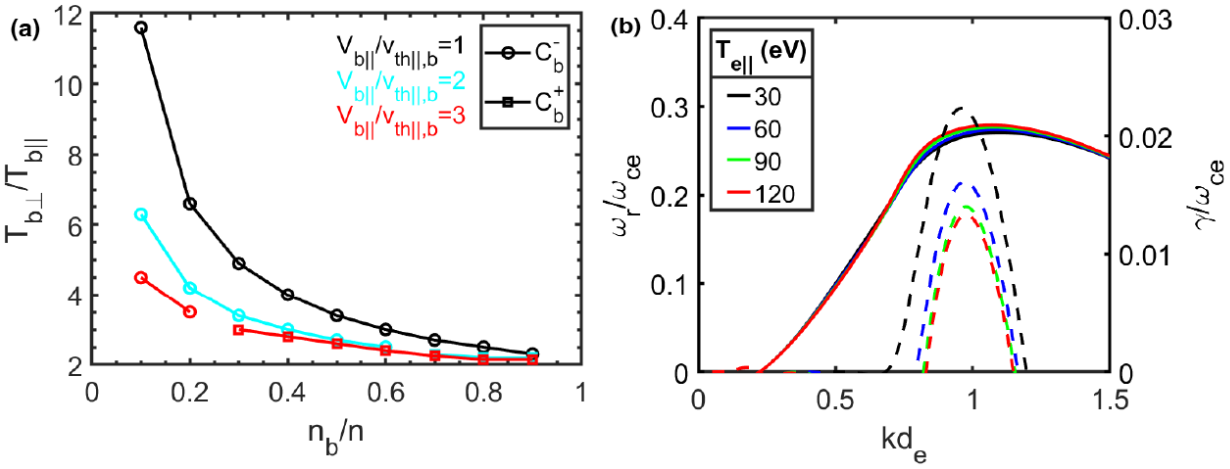

999

1000 **Figure 10.** The linear instability analysis for the competition between the background and beam
1001 populations. (a) Setting $T_{e\perp}/T_{e||}$=1, the critical $T_{b\perp}/T_{b||}$ that leads to the cyclotron mode growth
1002 rate reaching 0.005 ω_{ce} as a function of n_b/n and $V_{b||}/v_{th||,b}$. The modes propagating away from
1003 ('-') and toward ('+') the beam are marked with different symbols. The critical $T_{b\perp}/T_{b||}$ decreases
1004 with increasing n_b/n and $V_{b||}/v_{th||,b}$. (b) Dispersion curves for different $T_{e||}$, with other parameters
1005 fixed at n_b/n=0.7, $V_{b||}/v_{th||,b}$=1, $T_{e\perp}/T_{e||}$=1, and $T_{b\perp}/T_{b||}$=3. A smaller $T_{e||}$ allows for a higher
1006 growth rate, as it reduces the cyclotron damping effect.